NASA TECHNICAL MEMORANDUM

NASA TM X-1628

NASA TM X-1628

COMPARISON OF THEORETICAL AND EXPERIMENTAL PRESSURE DISTRIBUTIONS ON THE HL-10 MANNED LIFTING ENTRY VEHICLE AT MACH 10.5

by Charles L. Ladson and Peter T. Bernot

Langley Research Center
Langley Station, Hampton, Va.

NATIONAL AERONAUTICS AND SPACE ADMINISTRATION • WASHINGTON, D. C. • JULY 1968

NASA TM X-1628

COMPARISON OF THEORETICAL AND EXPERIMENTAL PRESSURE DISTRIBUTIONS ON THE HL-10 MANNED LIFTING ENTRY VEHICLE AT MACH 10.5

By Charles L. Ladson and Peter T. Bernot

Langley Research Center
Langley Station, Hampton, Va.

NATIONAL AERONAUTICS AND SPACE ADMINISTRATION

COMPARISON OF THEORETICAL AND EXPERIMENTAL PRESSURE DISTRIBUTIONS ON THE HL-10 MANNED LIFTING ENTRY VEHICLE AT MACH 10.5*

By Charles L. Ladson and Peter T. Bernot
Langley Research Center

SUMMARY

An investigation has been conducted in the Langley continuous-flow hypersonic tunnel at a Mach number of 10.5 to obtain pressure distributions over the windward surfaces of the HL-10 manned lifting entry vehicle. Data were obtained at angles of attack from 0^{o} to 60^{o} with elevon deflection angles from -60^{o} to 30^{o}. Most of the data were obtained at a Reynolds number of 1.5×10^{6} (based on model length), but for positive elevon deflection angles data were also obtained for Reynolds numbers of 1.1×10^{6} and 2.3×10^{6}.

The results of this investigation have been compared with modified Newtonian theory and tangent cone theory as well as other theories for isolated cases. In general, modified Newtonian theory gives a good first-order approximation to the magnitude and trends of both the longitudinal and lateral pressure distributions on the HL-10 vehicle for an elevon deflection angle of 0^{o}. However, there are areas in which the theory and experiment fail to agree. For example, the data show a spanwise pressure gradient over the flat lower surface at sideslip angles, appreciable values of pressure coefficient in the Newtonian "shadow region," and pressure gradients over the flat outer surface of the tip fin. At sideslip angles with the elevons deflected in a positive direction, large differential pressures exist between the windward and leeward elevons which induce large rolling moments on the vehicle. Also, for positive elevon deflection large amounts of separation exist ahead of the elevons and the theory is inadequate for predicting the pressure distribution over the elevons. Increasing the magnitude of the Reynolds number by a factor of 2 had a small and erratic effect on the pressure distribution over the elevons.

*Title, Unclassified.

INTRODUCTION

An investigation of a manned lifting entry vehicle having a maximum hypersonic lift-drag ratio of about 1 has been underway at the Langley Research Center since early 1962. The objective of these studies has been to expose problems and arrive at solutions in developing a configuration for lifting entry.

As a result of preliminary work, a configuration with negative camber, a flat bottom, a blunt leading edge, and a delta planform was selected for testing throughout the Mach number range and has been designated as HL-10. Aerodynamic results of this investigation, published in references 1 to 18, show that this body shape in combination with toed-in, rolled-out tip fins and a vertical center fin (designated I_4 and E_2, respectively, in the references) has static stability and is controllable throughout the range of test variables investigated for values of lift coefficient up to about 0.50. In tests at a Mach number of 10.5 the trim angle-of-attack range was from 27° to 51° for an elevon deflection range of -45° to 45° (ref. 18).

The pressure-distribution tests of the present investigation have also been conducted at a Mach number of 10.5 in the Langley continuous-flow hypersonic tunnel to supplement the force tests, to provide basic data for estimates of panel loads in full-scale vehicle studies, and to provide measurements for evaluation of theoretical methods. Data were obtained at angles of attack from 0° to 60° with elevon deflection angles from -60° to 30°. Some pressures at sideslip angles of 5° and 10° were also obtained during the test program. Most of the data were taken at a Reynolds number of 1.5×10^6 (based on model length), but for positive elevon deflection angles data were also recorded for Reynolds numbers of 1.1×10^6 and 2.3×10^6.

The data were recorded primarily for the windward surfaces of the body, elevons, and tip fins. Little data were obtained for the upper surface of the vehicle since it is shielded from the flow in the trim angle-of-attack range. All results are presented in tabular form along with summary plots of some of the more interesting trends noted in the data.

Additional pressure data on the HL-10 vehicle at hypersonic speeds are available in reference 1, but the configuration tested in this reference did not have the current tip fins. This factor should not affect the pressures on the body ahead of the fin location, however.

SYMBOLS

C_D drag coefficient, $\frac{\text{Drag}}{qS}$

C_L lift coefficient, $\frac{\text{Lift}}{qS}$

C_{l_β}	lateral stability parameter, per degree
C_m	pitching-moment coefficient, $\frac{\text{Pitching moment}}{qSl}$
C_{n_β}	directional stability parameter, per degree
C_p	pressure coefficient, $\frac{p_w - p_\infty}{q_\infty}$
$C_{p,max}$	maximum pressure coefficient
C_{Y_β}	side-force damping derivative, per degree
d	nose diameter
L/D	lift-drag ratio
l	model reference length (fig. 1)
M	Mach number
p	static pressure
p_t	stagnation pressure
p_w	static pressure at model wall
q	dynamic pressure
R	Reynolds number based on body length l
S	planform area
s	surface distance from plane of symmetry, positive for right side of model
T_t	stagnation temperature
X,Y,Z	model axis system
x,y,z	distances along longitudinal, lateral, and vertical axes (fig. 4)

α angle of attack, degrees

β angle of sideslip, degrees

γ ratio of specific heats

δ flow deflection angle

δ_e elevon deflection angle; angle between elevon surface and model surface ahead of elevon measured in plane normal to elevon hinge line; positive when trailing edge is down, degrees

Superscript:

' local conditions between model surface and shock

Subscripts:

1 settling chamber

2 conditions behind normal shock

∞ free-stream conditions

MODEL DESCRIPTION

A three-view drawing showing the basic dimensions of the HL-10 vehicle in combination with tip fins I_4 is presented in figure 1. This model, which is 12.0 inches (30.48 cm) long, is identical in size and geometry to the force model tested at M = 10.5 in reference 18 and detailed ordinates are presented in this reference. To obtain data throughout the angle-of-attack range from 0^o to 60^o, two different stings were used to mount the model on the tunnel support strut. The bent sting was used to obtain data at angles of attack of 0^o and 15^o, while the straight sting was used for angles of attack from 30^o to 60^o. Photographs and drawings of the two stings are presented in figures 2 and 3. Because the stings entered the vehicle on the upper surface, the center fin (designated E_2 in the references) was not in place for these tests. Inasmuch as the data obtained are mainly restricted to the lower surface of the vehicle and outer surface of the fins, neither the absence of the center fin nor the presence of the strut are believed to have any influence on the results.

The model was initially designed with 60 orifices on the surface. Some of these became blocked or inoperative during construction of the model and during configuration changes made in the tunnel. For such cases, either the orifice or the pressure coefficient for the orifice number has been omitted from the tabulated data. The locations of the orifices on the lower surface, elevon, base region, and upper surface are presented in figure 4. It should be noted that the main instrumentation is on the plane of symmetry of the vehicle and on the elevon. The four orifices ahead of the elevon (orifices 23, 25, 28, and 30) are essentially in line with the center row on the elevon, but on the opposite side of the vehicle; this arrangement was necessitated by the model construction. Since some data were obtained at sideslip angles, seven longitudinal stations were also instrumented and these orifice locations are presented in figure 5. The location of these orifices is presented in terms of the surface distance to the orifice from the lower-surface centerline s, divided by the vehicle nose diameter d. Positive values of s/d denote the right or windward side of the vehicle for positive sideslip angles. All orifices on the model had a diameter of 0.060 inch (0.152 cm).

The model and stings were constructed of stainless steel because of the high model-equilibrium temperatures expected during the tests. The model was also equipped with several thermocouples to measure the internal model-equilibrium temperature. The elevons were solid and were hinged so that the various deflection angles could be obtained by placing dowels in appropriate holes.

APPARATUS, TESTS, AND PROCEDURE

The data contained herein were obtained in the Mach 10 test section of the Langley continuous-flow hypersonic tunnel. This facility has a 31-inch-square (79-cm-square) test section and operates at stagnation pressures from about 20 to 150 atmospheres (2.03 MN/m^2 to 15.20 MN/m^2). A description and calibration of the facility is presented in the appendix of reference 18.

Tests were made at three stagnation pressures, and the following table presents the stagnation temperature, Mach number, and Reynolds number based on model length for each pressure:

$p_{t,1}$		$T_{t,1}$		M	R
psia	MN/m^2	^oR	^oK		
850	5.86	1760	978	10.41	1.1×10^6
1200	8.28	1790	994	10.46	1.5
1800	12.42	1880	1044	10.49	2.1

Most of the data were obtained at the intermediate stagnation pressure.

Because of the large angle-of-attack and stagnation-pressure ranges of the tests, each orifice was subjected to large changes in pressure. To provide more accurate data over the large pressure range, each orifice was connected to four pressure-measuring devices, each having a different range. For 0 to 0.56 psia (0 to 3.86 kN/m^2), an ionization-type pressure gage was used, and for higher pressures, standard electrical-type strain-gage pressure transducers having ranges of 0 to 1, 0 to 3, and 0 to 10 psia (0 to 6.89, 0 to 20.68, and 0 to 68.94 kN/m^2) were used. Data were recorded on all instrumentation simultaneously, but only the readings for the lowest range instrument which was still on scale have been presented. To reduce the amount of instrumentation needed to a reasonable value, scanner valves were used. By means of this valve, 11 orifices were connected to each set of four pressure-measuring devices and the valve was manually sequenced so that each of the 11 orifices was read out in order. The output of the instrumentation was visually displayed on a digital voltmeter as well as recorded on magnetic tape so that it could be determined when the pressures had reached an equilibrium value by watching the visual display before recording the data.

Three orifices on the model (orifices 14, 33, and 55) were exposed to very low pressures at all times and were directly connected to an ionization gage having a pressure range of 0 to 3 mm of mercury (0 to 399.9 N/m^2). At these low pressures, the data are subject to "thermal creep" effects as presented in reference 19. For example, at a stagnation pressure of 1200 psia (8.27 MN/m^2), a pressure equal to free-stream static pressure could be in error by 15 percent (0.003 psia, or 20.68 N/m^2) for the orifice diameter used and the approximately 1000° R (555° K) difference in temperature (as measured on model thermocouples) between the orifice and the pressure-measuring instrument. No corrections were applied since the exact temperature of each orifice is not known and the effects of tube length and local "hot spots" in the tubing on thermal creep are also unknown.

The pressure coefficients have been corrected for real-gas effects by the method presented in reference 20. The Mach numbers used in data reduction are also real-gas Mach numbers.

The accuracy of the strain-gage pressure transducers was better than ± 0.5 percent of the full-scale value, while the accuracy of the ionization gages is ± 2 percent of the actual reading. To account for zero shifts in the instrumentation, all gages were evacuated to a pressure of less than 10 microns of mercury (0.133 N/m^2) before each run and the increment between this zero value and the recorded pressure for each orifice was used in the data-reduction procedure.

PRESENTATION OF RESULTS

The results of this investigation are presented in tabular form, with summary plots of some of the more interesting trends. An index to the tables and summary figures follows:

δ_e, deg	R	Table
-60	1.5×10^6	I
-30	1.5	II
0	2.1	III
0	1.5	IV
15	2.1	V
15	1.5	VI
15	1.1	VII
30	2.1	VIII
30	1.5	IX
30	1.1	X

DISCUSSION

Comparison of Theory and Experiment for Undeflected Elevons

A comparison of experimental and theoretical lower-surface center-line pressure distributions is presented in figure 7 for an elevon deflection angle of 0°. Three theoretical methods were used in the analysis: modified Newtonian, modified Newtonian plus Prandtl-Meyer expansion, and tangent cone. For the modified Newtonian theory, the expression $C_p = C_{p,max} \sin^2 \delta$ $\left(\text{where } C_{p,max} = \frac{\gamma + 3}{\gamma + 1} \text{ from ref. 21}\right)$ was used. The modified Newtonian plus Prandtl-Meyer expansion obtained from reference 22 by using the recommended matching point technique wherein the Newtonian and Prandtl-Meyer pressure and pressure gradient are matched. For the tangent cone method, the values of pressure coefficient were obtained from reference 23.

In general, modified Newtonian theory predicts the trends in the data, but underestimates the magnitude. Modified Newtonian plus Prandtl-Meyer theory was used in an attempt to improve the agreement at the lower values of C_p. For a Mach number of 10.5, the matching point occurs at a C_p value of about 0.6, as seen in figure 7. This theory, however, overpredicts the experimental values on the aft end of the vehicle by a large amount. Tangent cone theory tends to give the best prediction at angles of attack of 0°, 15°, and 30°, but at the higher angles of attack it overpredicts the experiment by a considerable amount. The maximum pressure coefficient predicted by tangent cone theory is limited to the C_p at shock detachment which, for $M = 10.5$, is about 1.6. (See ref. 23.)

Although all theories used in comparison with the data were for an inviscid case, some viscous effects are noted on the model. For example, the lower surface of the HL-10, aft of $x/l = 0.75$, is parallel to the free stream at $\alpha = 15^{\circ}$. Thus, an inviscid pressure coefficient of zero is expected, while a measured value of about 0.03 is obtained. These viscous effects, although small, do contribute to the differences between theory and experiment.

Lateral pressure distributions at several longitudinal stations are presented in figures 8(a) to 8(g) for angles of attack of 0°, 30°, and 60° and sideslip angles of 0°, 5°, and 10°. The pressure coefficients are plotted against the nondimensional parameter s/d; positive values of s/d denote the right or windward side of the vehicle at positive sideslip angles. Cross-sectional drawings of the vehicle are also shown in each figure with tick marks to indicate the orifice locations.

The data in figure 8 are also compared with modified Newtonian theory for sideslip angles of 0° and 10°. The theoretical values of pressure coefficient were obtained by use of a high-speed digital computer program for the determination of the aerodynamic

characteristics of arbitrary three-dimensional shapes. For this program, the ordinates of about 200 points on the half-body, along with appropriate surface slopes for many of these points, were used to define the HL-10 shape. Although it is difficult to duplicate exactly an arbitrary three-dimensional shape on a computer program, the three-view drawings of the model plotted from the computer output agree very well with the actual model. The lower-surface center-line pressure distributions from the computer program are consistent with the hand-calculated values.

The theoretical and experimental results in figure 8 show that C_p from modified Newtonian theory becomes zero at a lower value of s/d than the experimental C_p. This is probably the result of blunt-body "blast wave" effects producing a higher inviscid pressure as well as to some small viscous effects. Modified Newtonian theory plus Prandtl-Meyer expansion theory (ref. 22) was used in figure 8(a) in an effort to improve the predictions. At $\alpha = 0^o$ this theory gives high values for all orifices except the one on the upper-surface center line. Although this orifice is "shielded" by Newtonian flow assumptions, the Prandtl-Meyer expansion shows good agreement with the experimental pressure for this location. At $\alpha = 30^o$ and 60^o, this theory also shows better agreement than Newtonian alone for the pressure in the low pressure-coefficient range. Since this theory shows poor agreement with the experimental distribution on the lower-surface center line (fig. 7), it was applied only to the $x/l = 0.125$ station.

Although the modified Newtonian theory obtained from the computer program gives very good first-order engineering approximations to the aerodynamic characteristics, several areas of differences between theory and experiment are noted. This is to be expected when such a simplified theoretical approach is used. Differences in center-line pressure distribution and in the location where zero pressure coefficient is obtained on the vehicle have already been mentioned. Another difference between theory and experiment is shown best in figures 8(c) and 8(d). Theory predicts a loss in pressure coefficient on the flat portion of the lower surface of the vehicle as sideslip angle is increased from 0^o to 10^o for angles of attack at which the aft protion of the lower surface is not shielded from the flow. Experimental values of pressure coefficient, however, show an increase with sideslip angle on the windward side of the center line and a decrease on the leeward side. Since the windward leading edge builds up a high pressure at sideslip angles, while the leeward leading edge loses pressure, it is obvious that the pressure gradient across the model must exist. The gradient also seems to increase as the angle of attack increases, since the maximum lateral pressure coefficient moves closer to the tangency point between the flat bottom and curved sides as the angle of attack increases.

For the tests at $\alpha = 0^o$, the model support sting was exposed to the flow and probably caused some interference with the flow over the tip fin. Evidence of this can be seen in figure 8(e) where the leading-edge orifice shows a value of C_p of about 1.85; such a value is very unlikely unless there was shock interference from the sting. Elevated

pressures on the shielded inner surface of the fin at $\alpha = 0^{\circ}$ (figs. 8(e), 8(f), and 8(g)) also suggest sting interference. At the other angles of attack, however, the sting is shielded from the flow, as seen in figure 6, and all data should be interference free.

Detailed differences between theory and experiment are noted on the outer surface of the tip fins. Since this is a flat surface, theory gives constant values of C_p over the fins, as shown in figures 8(e), 8(f), and 8(g). The experimental pressure is not constant over the flat fin surface, and seems to be influenced, not only by the pressure on the model lower surface, but also by the proximity of the orifice to the fin leading edge. The magnitudes of the pressure coefficients, as well as some of the increments between 0° and 10° sideslip angles, are not predicted with very good accuracy for either the windward or leeward fin.

The computer program used to obtain the detailed pressure distributions also provided the integrated forces and moments on the vehicle. These results are compared in figure 9 with the force data obtained at $M = 10.5$ (from ref. 18). Figure 9(a) shows very good agreement between the theoretical and experimental longitudinal characteristics. For example, the theory predicts the trim angle of attack (for 0° elevon deflection) within 1°, the maximum lift-drag ratio within about 5 percent, and the maximum lift coefficient within about 7 percent. Figure 9(b), however, shows that the lateral and directional stability parameters C_{l_β} and C_{n_β} are very poorly predicted, although the theoretical side-force damping derivative C_{Y_β} shows good agreement with the experimental data.

Some of the differences between theory and experiment can be explained by the trends noted in figure 8. For example, the experimental lateral pressure gradient over the lower surface of the vehicle at the higher angles of attack would both increase the lateral stability and decrease the directional stability from the theoretical values. Likewise, the differences in the lateral location of zero pressure coefficient on the body, as well as differences between the theoretical and experimental values of pressure coefficient on the tip fins, would cause large changes in the directional and lateral characteristics but have little effect on the longitudinal data.

In summary, these data illustrate the ability of this type of computer program and Newtonian theory to give good first-order approximations to the longitudinal force characteristics of a complex vehicle at zero elevon deflection and also show that the directional and lateral stability characteristics obtained from the program may be in error by substantial amounts. The detailed pressure distributions indicate several reasons for the disagreement between theory and experiment for these lateral characteristics.

Comparison of Theory and Experiment With Elevons Deflected

Isometric sketches presenting the pressure coefficients for the elevons at various deflection angles, the four orifices ahead of the elevons, and the lower-surface center line

from $x/\ell = 0.625$ aft are shown in figures 10(a) to 10(d) for angles of attack of 30^o, 40^o, 50^o, and 60^o, respectively. For an elevon deflection angle of 0^o, the pressure coefficient is essentially constant over the flat portion of the lower surface (aft of $x/\ell = 0.75$), as was indicated in figure 7. For elevon deflection angles of -30^o and -60^o, pressure coefficients as large as 0.065 (six times stream static pressure) were measured on the elevon for angles of attack at which the elevon was in the Newtonian shadow region by 5^o to 15^o. Examples of such values are seen for $\delta_e = -30^o$ at $\alpha = 40^o$ (fig. 10(b)) and $\delta_e = -60^o$ at 60^o (fig. 10(d)). Although these pressure coefficients are small, they are much higher than would be expected in this expansion region and are probably caused by the high-pressure region surrounding the elevon feeding over onto the elevon surface. For the extreme expansion angles encountered in these tests (for example, 45^o at $\delta_e = -60^o$ and $\alpha = 30^o$), the pressure on the elevon is essentially equal to stream static pressure. Indications of high-shear regions on the elevon have previously been noted in oil-flow photographs and incremental pitching moments at $M = 6.8$ (ref. 4) and in the incremental pitching moment at $M = 10.5$ (ref. 18).

The effect of the pressure field around the elevon on the elevon pressures is also shown by comparing the results for $\delta_e = 0^o$ at $\alpha = 30^o$ (fig. 10(a)) with data for $\delta_e = -30^o$ at $\alpha = 60^o$ (fig. 10(d)). Although the Newtonian flow-deflection angle (15^o) is the same for both these cases, the high-pressure field around the elevon at $\alpha = 60^o$ causes elevon pressures which are about three times as high as those at the lower angles of attack. This indicates that Newtonian concepts for the pressures on elevons are not applicable even in the simple case where no separated flow exists.

When the elevons are deflected into the flow (positive elevon deflection angles), separation may occur ahead of the elevon and affect the elevon pressures. Oil-flow photographs for $\delta_e = 30^o$ at Mach numbers of 20.3 in helium and 6.8 in air (ref. 2) and schlieren flow photographs at $M = 6.8$ (ref. 4) show the extent of separation on the HL-10 vehicle. The shadowgraphs made during the present tests are not of good enough quality to show separation regions and no oil-flow photographs were obtained. Thus, it is difficult to visualize the actual flow pattern over the elevons from the pressure distributions alone.

Much information has been published on flow separation ahead of flaps on two-dimensional flat plates and on flat-plate delta wings. (See refs. 24 to 27.) These are simple types of flow separation when compared with the flow field over the HL-10, however. This vehicle, with its highly cambered lower surface, provides a very strong longitudinal pressure gradient ahead of the elevons (see fig. 7). Also, the swept elevon hinge lines and rolled-out tip fins located near the elevon tip chord can produce strong cross-flow effects not observed on the simpler configurations. In general, at $\alpha = 30^o$ and 40^o (figs. 10(a) and 10(b)), laminar separation appears to have occurred ahead of the elevons

for both $\delta_e = 15^o$ and $\delta_e = 30^o$. This separation is evidenced by an increase in pressure ahead of the elevon and along the vehicle center line as compared with the $\delta_e = 0^o$ case. Since no second plateau pressure is obtained, the flow probably does not reattach close enough to the hinge line for the second plateau to form. At angles of attack of 50^o and 60^o (figs. 10(c) and 10(d)), the pressure reaches a peak in the middle of the elevon and then decreases toward the trailing edge. Since a pressure rise occurs ahead of the elevon, laminar separation is again indicated, although the distribution over the elevon is typical of turbulent separation. Thus, there is an indication that transition may have occurred in the separated region, although with the complex flow field being considered, this is only a possible explanation of the trends in the data.

The pressure distributions over the elevons for an angle of attack of 30^o and an elevon deflection angle of 30^o are presented in figure 11 for sideslip angles of 5^o and 10^o. Although Newtonian theory predicts higher pressures on the leeward elevon (because of the swept hinge line), the experimental data show substantially higher loading on the windward elevon. This is probably the result of the previously noted spanwise pressure gradient at sideslip angles feeding onto the elevon. This differential loading on the elevons explains the large increase in lateral stability with increasing positive elevon deflection angle noted in reference 18.

In an attempt to define the flow field in which the elevons operate and to improve the ability to calculate deflected-elevon pressures, a total-pressure survey was made in a vertical plane with the model at an angle of attack of 30^o and an elevon deflection of 0^o. The survey was made at $x/l = 0.812$ (when probe was at model surface), and at y/l values of 0, 0.074, and 0.148. Since the probe moved in a vertical plane while the model was at an angle of attack of 30^o, the x/l location of the probe with respect to the model increased as the probe was moved away from the model surface. Results of this survey, shown in figure 12, indicate that the ratio of local to free-stream total pressure varies between the model surface and the bow-shock wave. In similar tests at $M = 10.1$ on a blunt 70^o swept flat-plate delta wing (ref. 28), this ratio was essentially constant between the body and shock wave. The fact that the shock wave is located closer to the body surface as y/l increases (fig. 12) is an indication of the three-dimensional nature of the flow.

The static pressure on the model at $x/l = 0.812$ and the measured total pressure were used to calculate the local Mach number and the ratio of local to free-stream dynamic pressure. At the edge of the boundary layer, the Mach number is about 3 and the ratio of local to free-stream dynamic pressure is about 1. When the elevons are deflected into the stream, however, separation occurs well ahead of the elevon. (See fig. 10.) No surveys have been made in the separated region.

To provide an indication of the ability to predict the pressure on the elevon when it is deflected in the positive direction, the pressures for the four orifices ahead of the elevon and the center row of orifices on the elevon are presented in figure 13 for angles of attack of 30°, 40°, 50°, and 60°, at the three Reynolds numbers of the investigation. The effects of Reynolds number on the data are, in general, small and inconsistent over the small range of these tests. No effects of Reynolds number are discernible in the shadowgraphs presented in figure 14. Although there is a large pressure gradient over the elevon resulting from the separated flow, the inviscid theories give a constant level for the elevon pressure. Three methods – modified Newtonian theory, tangent cone theory, and the results from reference 29 – have been used to predict the level of the pressure. For the case of $\delta_e = 0^{\circ}$ at $\alpha = 30^{\circ}$ where the flow survey was made, an oblique-shock calculation was also made on the basis of the Mach number at the edge of the boundary layer. From the results shown in figure 13, it is obvious that the pressure distribution along elevons cannot be predicted by using these simple theories. Only general levels can be computed, whereas the actual distribution is a function of the vehicle shape ahead of the elevons, the nature of the boundary layer, the sweep of the elevon hinge line, and the local Reynolds number. Although much effort is being devoted to both theoretical and experimental surveys for the two-dimensional case, the complex three-dimensional case still remains a large problem area.

CONCLUDING REMARKS

An investigation has been conducted in the Langley continuous-flow hypersonic tunnel at a Mach number of 10.5 to obtain pressure distributions over the windward surfaces of the HL-10 manned lifting entry vehicle. Data were obtained at angles of attack from 0° to 60° with elevon deflection angles from -60° to 30°. Most of the data were obtained at a Reynolds number of 1.5×10^6 (based on model length), but for positive elevon deflection angles data were also obtained for Reynolds numbers of 1.1×10^6 and 2.3×10^6.

The results of this investigation have been compared with modified Newtonian theory and tangent cone theory as well as other theories for isolated cases. In general, modified Newtonian theory gives a good first-order approximation to the magnitude and trends of both the longitudinal and lateral pressure distributions on the HL-10 configuration for an elevon deflection angle of 0°. However, there are areas in which the theory and experiment fail to agree; for example, the data show a spanwise pressure gradient over the flat lower surface at sideslip angles, appreciable values of pressure coefficient in the Newtonian shadow region, and pressure gradients over the flat outer surface of the tip fin. Likewise, at sideslip angles with the elevons deflected in a positive direction, large differential pressures exist between the windward and leeward elevons which induce large rolling moments on the vehicle. Also, for positive elevon deflection large amounts of

separation exist ahead of the elevons and the theory is inadequate for predicting the pressure distribution over the elevons. Increasing the magnitude of the Reynolds number by a factor of 2 had a small and erratic effect on the pressure distribution over the elevons.

Langley Research Center,
National Aeronautics and Space Administration,
Langley Station, Hampton, Virginia, January 15, 1968,
124-07-02-56-23.

REFERENCES

1. Harvey, William D.: Pressure Distribution on HL-10 Manned Lifting Entry Vehicle at a Mach Number of 19.5. NASA TM X-1135, 1965.

2. Johnston, Patrick J.: Stability Characteristics of a Manned Lifting Entry Vehicle at a Mach Number of 20.3 in Helium. NASA TM X-1156, 1965.

3. Spencer, Bernard, Jr.: An Investigation of Methods of Improving Subsonic Performance of a Manned Lifting Entry Vehicle. NASA TM X-1157, 1965.

4. Ladson, Charles L.: Aerodynamic Characteristics of a Manned Lifting Entry Vehicle With Modified Tip Fins at Mach 6.8. NASA TM X-1158, 1965.

5. Rainey, Robert W.: Summary of an Advanced Manned Lifting Entry Vehicle Study. NASA TM X-1159, 1965.

6. Ware, George M.: Full-Scale Wind-Tunnel Investigation of the Aerodynamic Characteristics of the HL-10 Manned Lifting Entry Vehicle. NASA TM X-1160, 1965.

7. Harris, Charles D.: Effect of Elevon Deflection and of Model Components on Aerodynamic Characteristics of a Manned Lifting Entry Vehicle at Mach Numbers of 0.20 to 1.20. NASA TM X-1226, 1966.

8. Spencer, Bernard, Jr.; and Fox, Charles H., Jr.: Subsonic Longitudinal Control Characteristics of Several Elevon Configurations for a Manned Lifting Entry Vehicle. NASA TM X-1227, 1966.

9. Harris, Charles D.: Control-Surface Hinge-Moment and Elevon Normal-Force Characteristics at Transonic Speeds on a Manned Lifting Entry Vehicle. NASA TM X-1241, 1966.

10. Harris, Charles D.: Transonic Aerodynamic Characteristics of a Manned Lifting Entry Vehicle With and Without Tip Fins. NASA TM X-1248, 1966.

11. Campbell, James F.; and Watson, Carolyn B.: Stability and Control, Hinge-Moment, and Pressure-Coefficient Data for the HL-10 Manned Lifting Entry Vehicle at Mach Numbers From 1.41 to 2.16. NASA TM X-1300, 1966.

12. Ware, George M.: Investigation of the Flight Characteristics of a Model of the HL-10 Manned Lifting Entry Vehicle. NASA TM X-1307, 1967.

13. Campbell, James F.; and Grow, Josephine W.: Stability and Control Characteristics of a Manned Lifting Entry Vehicle at Mach Numbers From 1.50 to 2.16 Including Hinge Moment and Pressure Distribution Data. NASA TM X-1314, 1966.

14. Ladson, Charles L.: Effects of Various Canopies on the Aerodynamic Characteristics of a Manned Lifting Entry Vehicle at Mach 0.06 to 6.8. NASA TM X-1321, 1966.

15. Johnson, Joseph L., Jr.; Chambers, Joseph R.; and White, Lucy C.: Analytical Study of the Subsonic Dynamic Stability and Response of the HL-10 Entry Vehicle. NASA TM X-1348, 1967.

16. Henderson, William P.: Static Stability Characteristics of a Manned Lifting Entry Vehicle at High Subsonic Speeds. NASA TM X-1349, 1967.

17. Spencer, Bernard, Jr.: Effects of Elevon Planform on Low-Speed Aerodynamic Characteristics of the HL-10 Manned Lifting Entry Vehicle. NASA TM X-1409, 1967.

18. Ladson, Charles L.: Aerodynamic Characteristics of the HL-10 Manned Lifting Entry Vehicle at a Mach Number of 10.5. NASA TM X-1504, 1968.

19. Arney, G. D., Jr.; and Bailey, A. B.: Addendum to an Investigation of the Equilibrium Pressure Along Unequally Heated Tubes. AEDC-TDR-62-188, U.S. Air Force, Oct. 1962.

20. Erickson, Wayne D.; and Creekmore, Helen S.: A Study of Equilibrium Real-Gas Effects in Hypersonic Air Nozzles, Including Charts of Thermodynamic Properties for Equilibrium Air. NASA TN D-231, 1960.

21. Lees, Lester: Hypersonic Flow. Fifth Intern. Aeron. Conf. (Los Angeles, Calif.), Inst. Aeron. Sci., Inc., June 1955, pp. 241-276.

22. Kaufman, Louis G., II: Pressure Estimation Techniques for Hypersonic Flows Over Blunt Bodies. J. Astronaut. Sci., vol. X, no. 2, Summer 1963, pp. 35-41.

23. Ames Research Staff: Equations, Tables, and Charts for Compressible Flow. NACA Rept. 1135, 1953. (Supersedes NACA TN 1428.)

24. Sterrett, James R.; and Emery, James C.: Experimental Separation Studies for Two-Dimensional Wedges and Curved Surfaces at Mach Numbers of 4.8 to 6.2. NASA TN D-1014, 1962.

25. Putnam, Lawrence E.: Investigation of Effects of Ramp Span and Deflection Angle on Laminar Boundary-Layer Separation at Mach 10.03. NASA TN D-2833, 1965.

26. Townsend, James C.: Effects of Leading-Edge Bluntness and Ramp Deflection Angle on Laminar Boundary-Layer Separation in Hypersonic Flow. NASA TN D-3290, 1966.

27. Kaufman, Louis G., II; Meckler, Lawrence; Hartofilis, Stavros A.; and Weiss, Daniel: An Investigation of Hypersonic Flow Separation and Control Characteristics. AFFDL-TR-64-174, U.S. Air Force, Jan. 1965.

28. Rhudy, J. P.; and Carman, J. B., Jr.: Pitot Pressure Survey of the Flow Field of a 70-Deg Swept Blunted Delta Wing at Angle of Attack. AEDC-TR-65-231, U.S. Air Force, Nov. 1965. (Available from DDC as AD 473 713.)

29. Fetterman, David E.: A Method for Predicting the Normal-Force Characteristics of Delta Wings at Angles of Attack From 0° to 90°. NASA TM X-757, 1963.

TABLE I.- PRESSURE COEFFICIENTS FOR $\delta_e = -60^o$ AND $R = 1.5 \times 10^6$

Orifice	C_p at α =					
	30^o	40^o	50^o	60^o		
	$\beta = 0^o$			$\beta = 0^o$	5^o	10^o
1	1.3787	1.0624	0.6992	0.4037	0.4028	0.4020
2	1.4064	1.6970	1.8894	1.9501	1.9476	1.8774
3	0.0359	0.0114	0.0091	0.0051	0.0053	0.0043
4	1.1148	1.4729	1.7523	1.9129	1.9016	1.8697
5	0.5416	0.6107	0.6480	0.6242	0.7407	0.8799
6	0.2147	0.2225	0.2171	0.2015	0.2583	0.3304
7	0.0906	0.0897	0.0935	0.0879	0.1073	0.1442
8	0.0292	0.0307	0.0400	0.0394	0.0045	0.0043
9	0.8098	1.1600	1.4962	1.7458	1.7366	1.7166
10	0.4406	0.5275	0.5763	0.5788	0.6985	0.8308
11	0.2036	0.2120	0.2095	0.1948	0.2528	0.3237
12	0.1104	0.1136	0.1101	0.1008	0.1345	0.1802
13	0.0017	-0.0002	0.0150	0.0019	0.0012	0.0014
14	0.0094	0.0050	0.0036	0.0028	0.0026	0.0018
15	0.5530	0.8786	1.2284	1.5264	1.5221	1.5126
16	0.3163	0.5799	0.9086	1.2561	1.2521	1.2485
17	0.3179	0.5827	0.9143	1.2599	1.2823	1.2992
18	0.2578	0.3363	0.4013	0.4438	0.5559	0.6870
19	0.1611	0.1575	0.1507	0.1424	0.1986	0.2708
20	0.0779	0.0773	0.0666	0.0584	0.0855	0.1204
21	0.2388	0.4683	0.7770	1.1375	1.1334	1.1338
22	0.2027	0.4165	0.7239	1.1002	1.0969	1.0992
23	0.2217	0.4386	0.7365	1.0826	1.1429	1.2024
24	0.1749	0.3759	0.6791	1.0607	1.0585	1.0612
25	0.1917	0.3995	0.6986	1.0550	1.1056	1.1547
26	0.1507	0.3410	0.6393	1.0204	1.0185	1.0202
27	0.1556	0.3484	0.6451	1.0218	1.0437	1.0646
28	0.1634	0.3579	0.6525	1.0155	1.0553	1.0989
29	0.1410	0.3307	0.6355	1.0261	1.0258	1.0262
30	0.1521	0.3447	0.6510	1.0334	1.0691	1.1074
31	0.1362	0.3281	0.6466	1.0460	1.0474	1.0497
32	0.1261	0.3177	0.6361	1.0073	1.0042	1.0013
33	-0.0030	-0.0020	-0.0018	0.0003	-0.0002	0.0006
34	-0.0066	0.0030	0.0212	0.0613	0.0597	0.0551
35	-0.0089	-0.0037	0.0064	0.0302	0.0212	0.0209
36	-0.0069	0.0007	0.0153	0.0551	0.0557	0.0560
37	-0.0059	-0.0012	0.0114	0.0403	0.0374	0.0324
38	-0.0061	-0.0017	0.0012	0.0156	0.0156	0.0160
39	-0.0066	-0.0028	0.0050	0.0353	0.0360	0.0345
40	-0.0047	-0.0012	0.0032	0.0190	0.0137	0.0126
41	-0.0055	-0.0001	0.0019	0.0143	0.0143	0.0150
42	-0.0054	-0.0003	0.0002	0.0213	0.0305	0.0333
43	0.1687	0.3607	0.6443	0.9827	0.9202	0.8677
44	0.1939	0.3188	0.4614	0.5881	0.4600	0.3517
45	0.0196	0.0259	0.0473	0.0328	0.0087	0.0298
46	0.1619	0.2466	0.3495	0.4080	0.2939	0.2091
47	0.1457	0.1651	0.1858	0.1863	0.1150	0.0708
48	0.1474	0.1533	0.1487	0.1555	0.1055	0.0637
49	0.1456	0.0597	0.0117	0.0013	0.0043	0.0065
50	-0.0050	-0.0030	0.0003	0.0083	0.0070	0.0084
52	0.1436	0.1490	0.1632	0.1830	0.1241	0.0750
53	0.0131	-0.0002	-0.0029	0.0139	0.0060	0.0065
54	-0.0063	-0.0029	-0.0005	0.0053	0.0062	0.0069
55	-0.0065	-0.0059	0.0013	0.0127	0.0108	0.0089
56	0.1385	0.1625	0.1660	0.1536	0.0890	0.0426
57	0.1394	0.1539	0.1725	0.1805	0.1146	0.0672
59	-0.0041	-0.0012	-0.0004	0.0050	0.0064	0.0074
60	-0.0046	-0.0027	-0.0013	0.0038	0.0057	0.0063

TABLE II.- PRESSURE COEFFICIENTS FOR $\delta_e = -30^o$ AND $R = 1.5 \times 10^6$

Orifice	C_p at α =			
	30^o	40^o	50^o	60^o
	$\beta = 0^o$			
1	1.3295	1.0335	0.6806	0.3930
2	1.3631	1.6534	1.8458	1.8965
3	0.0292	0.0109	0.0073	0.0054
4	1.0864	1.4328	1.7111	1.8707
5	0.5277	0.5997	0.6322	0.6080
6	0.2161	0.2177	0.2136	0.1984
7	0.0882	0.0847	0.0824	0.0768
8	0.0167	0.0120	0.0076	0.0043
9	0.7722	1.1311	1.4537	1.7100
10	0.4263	0.5077	0.5556	0.5607
11	0.1985	0.2070	0.2039	0.1905
12	0.1075	0.1112	0.1070	0.0957
13	0.0021	0.0001	-0.0014	-0.0002
14	0.0094	0.0050	0.0035	0.0027
15	0.5353	0.8575	1.2015	1.4945
16	0.3056	0.5660	0.8892	1.2313
17	0.3092	0.5678	0.8896	1.2303
18	0.2516	0.3293	0.3931	0.4360
19	0.1555	0.1536	0.1485	0.1395
20	0.0747	0.0717	0.0653	0.0572
21	0.2302	0.4582	0.7590	1.1156
22	0.1954	0.4084	0.7089	1.0803
23	0.2153	0.4288	0.7210	1.0621
24	0.1695	0.3697	0.6668	1.0421
25	0.1862	0.3916	0.6840	1.0369
26	0.1467	0.3355	0.6269	1.0039
27	0.1507	0.3414	0.6307	1.0028
28	0.1586	0.3517	0.6388	0.9976
29	0.1379	0.3262	0.6243	1.0096
30	0.1475	0.3391	0.6381	1.0165
31	0.1325	0.3227	0.6351	1.0313
32	0.1256	0.3139	0.6255	0.9928
33	-0.0048	-0.0037	-0.0024	-0.0004
34	0.0183	0.0647	0.1556	0.2894
35	0.0112	0.0456	0.1114	0.2057
36	0.0178	0.0625	0.1471	0.2787
37	0.0125	0.0506	0.1333	0.2804
38	0.0080	0.0301	0.0940	0.1968
39	0.0058	0.0445	0.1295	0.2785
40	0.0058	0.0410	0.1290	0.2702
41	-0.0007	0.0212	0.0876	0.1950
42	0.0006	0.0328	0.1278	0.3313
43	0.1650	0.3542	0.6313	0.9636
44	0.1903	0.3137	0.4529	0.5788
45	0.0262	-0.0016	0.0030	0.0061
46	0.1610	0.2407	0.3304	0.3929
47	0.1406	0.1624	0.1847	0.1968
48	0.1466	0.1504	0.1395	0.1514
49	0.1438	0.0487	0.0051	0.0005
50	-0.0045	-0.0003	0.0034	0.0055
52	0.1406	0.1501	0.1602	0.1815
53	0.0119	0.0004	-0.0005	0.0026
54	-0.0047	0.0003	0.0034	0.0049
55	-0.0074	-0.0055	0.0012	0.0129
56	0.1373	0.1620	0.1678	0.1488
57	0.1348	0.1511	0.1707	0.1820
59	-0.0031	0.0013	0.0034	0.0051
60	-0.0026	0.0000	0.0028	0.0049

TABLE III.- PRESSURE COEFFICIENTS FOR $\delta_e = 0^\circ$ AND $R = 2.1 \times 10^6$

Orifice	C_p at α =					
	0°	15°	30°	40°	50°	60°
	$\beta = 0^\circ$					
1	1.8808	1.7313	1.3289	1.0292	0.6676	0.3873
2	0.4260	0.9016	1.3599	1.6272	1.8171	1.8554
3	0.1937	0.0633	0.0258	0.0089	0.0074	0.0047
4	0.2243	0.5888	1.0911	1.4214	1.6634	1.8106
5	0.2378	0.3980	0.5373	0.6019	0.6286	0.6069
6	0.1672	0.1911	0.2083	0.2152	0.2115	0.1935
7	0.1290	0.1006	0.0858	0.0837	0.0810	0.0737
8	0.0672	0.0277	0.0178	0.0107	0.0063	0.0031
9	0.0943	0.3558	0.7736	1.1319	1.4409	1.6644
10	0.1610	0.2997	0.4289	0.5107	0.5519	0.5554
11	0.1520	0.1889	0.1979	0.2045	0.2002	0.1858
12	0.1225	0.1108	0.1069	0.1096	0.1051	0.0927
13	0.0555	0.0194	0.0002	-0.0016	-0.0024	-0.0024
14	0.0455	0.0206	0.0092	0.0046	0.0029	0.0018
15	0.0391	0.1972	0.5386	0.8552	1.1735	1.4613
16	0.0107	0.0879	0.3072	0.5687	0.8810	1.2079
17	0.0102	0.0894	0.3122	0.5741	0.8830	1.2052
18	0.0630	0.1493	0.2495	0.3250	0.3837	0.4248
19	0.1353	0.1507	0.1553	0.1508	0.1444	0.1345
20	0.1199	0.0876	0.0753	0.0714	0.0646	0.0552
21	0.0036	0.0573	0.2336	0.4588	0.7508	1.0935
22	-0.0002	0.0418	0.1982	0.4069	0.7006	1.0604
23	-0.0037	0.0497	0.2163	0.4320	0.7192	1.0529
24	-0.0022	0.0326	0.1702	0.3670	0.6582	1.0237
25	-0.0048	0.0393	0.1857	0.3904	0.6799	1.0269
26	-0.0038	0.0245	0.1460	0.3330	0.6201	0.9903
27	-0.0034	0.0280	0.1500	0.3395	0.6286	0.9945
28	-0.0066	0.0295	0.1586	0.3491	0.6348	0.9900
29	-0.0046	0.0206	0.1366	0.3252	0.6199	0.9987
30	-0.0076	0.0246	0.1481	0.3370	0.6341	1.0010
31	-0.0056	0.0183	0.1317	0.3203	0.6283	1.0079
32	-0.0046	0.0166	0.1277	0.3160	0.6308	1.0124
33	-0.0045	-0.0014	-0.0051	-0.0030	-0.0025	0.0018
34	-0.0074	0.0168	0.1250	0.3106	0.6244	0.9975
35	-0.0089	0.0182	0.1297	0.3140	0.6193	0.9833
36	-0.0095	0.0213	0.1445	0.3349	0.6304	0.9652
37	-0.0075	0.0165	0.1234	0.3093	0.6239	0.9983
38	-0.0085	0.0173	0.1265	0.3115	0.6186	0.9810
39	-0.0088	0.0201	0.1363	0.3235	0.6191	0.9622
40	-0.0078	0.0081	0.1099	0.2831	0.5803	0.9293
41	-0.0087	0.0093	0.1144	0.2878	0.5768	0.9121
42	-0.0088	0.0157	0.1239	0.3017	0.5854	0.9035
43	0.0015	0.0325	0.1651	0.3558	0.6301	0.9557
44	0.0091	0.0627	0.1923	0.3160	0.4601	0.5833
45	0.0532	0.0055	-0.0012	-0.0023	0.0026	0.0042
46	0.0206	0.0547	0.1624	0.2407	0.3295	0.3943
47	0.1284	0.1179	0.1466	0.1623	0.1826	0.1958
48		0.1397	0.1467	0.1493	0.1384	0.1466
49	1.9331	0.5428	0.1414	0.0495	0.0174	0.0001
50	0.1604	0.0046	-0.0067	0.0002	0.0032	0.0043
52	0.1119	0.1620	0.1433	0.1491	0.1597	0.1827
53	0.2048	0.0874	0.0106	-0.0009	0.0003	0.0027
54	0.0982	0.0010	-0.0050	0.0006	0.0030	0.0047
55	-0.0074	-0.0043	-0.0035	-0.0045	0.0039	0.0218
56	0.1006	0.1052	0.1390	0.1632	0.1689	0.1459
57	0.0987	0.1334	0.1358	0.1513	0.1714	0.1854
59	0.0363	-0.0033	-0.0022	0.0019	0.0036	0.0048
60	-0.0027	-0.0032	-0.0021	-0.0003	0.0014	0.0022

TABLE IV.- PRESSURE COEFFICIENTS FOR $\delta_e = 0^o$ AND $R = 1.5 \times 10^6$

Orifice	C_p at α =					
	0^o	15^o	30^o	40^o	50^o	60^o
	$\beta = 0^o$					
1	1.8603	1.7393	1.3548	1.0220	0.6712	0.3957
2	0.4220	0.8964	1.4123	1.6232	1.8055	1.8687
3	0.1951	0.0667	0.0182	0.0100	0.0079	0.0059
4	0.2260	0.5886	1.1264	1.4177	1.6676	1.8331
5	0.2360	0.3960	0.5415	0.5940	0.6325	0.6117
6	0.1675	0.1907	0.2152	0.2162	0.2140	0.1987
7	0.1300	0.1010	0.0883	0.0845	0.0833	0.0769
8	0.0687	0.0311	0.0157	0.0115	0.0069	0.0038
9	0.0958	0.3545	0.8039	1.1204	1.4360	1.6913
10	0.1595	0.2978	0.4328	0.5031	0.5523	0.5586
11	0.1507	0.1901	0.2030	0.2078	0.2032	0.1926
12	0.1228	0.1124	0.1114	0.1115	0.1072	0.0962
13	0.0573	0.0179	0.0018	-0.0011	-0.0015	-0.0004
14	0.0468	0.0206	0.0092	0.0050	0.0034	0.0028
15	0.0404	0.1964	0.5548	0.8483	1.1819	1.4743
16	0.0112	0.0882	0.3235	0.5570	0.8804	1.2150
17	0.0107	0.0898	0.3271	0.5624	0.8724	1.2217
18	0.0846	0.1497	0.2578	0.3220	0.3910	0.4296
19	0.1342	0.1514	0.1611	0.1526	0.1476	0.1390
20	0.1208	0.0894	0.0783	0.0718	0.0656	0.0566
21	0.0043	0.0580	0.2422	0.4498	0.7520	1.0937
22	0.0006	0.0424	0.2032	0.3993	0.7007	1.0585
23	-0.0026	0.0497	0.2274	0.4249	0.7117	1.0538
24	-0.0016	0.0333	0.1803	0.3601	0.6557	1.0200
25	-0.0046	0.0400	0.1968	0.3861	0.6774	1.0292
26	-0.0035	0.0251	0.1542	0.3275	0.6155	0.9841
27	-0.0026	0.0284	0.1597	0.3364	0.6180	0.9956
28	-0.0059	0.0303	0.1665	0.3458	0.6340	0.9878
29	-0.0043	0.0211	0.1433	0.3186	0.6176	0.9942
30	-0.0068	0.0253	0.1556	0.3325	0.6303	0.9964
31	-0.0051	0.0186	0.1388	0.3156	0.6152	1.0150
32	-0.0044	0.0172	0.1349	0.3114	0.6162	1.0090
33	-0.0043	-0.0005	-0.0023	-0.0035	-0.0025	0.0027
34	-0.0071	0.0130	0.1345	0.3026	0.6051	0.9994
35	-0.0083	0.0146	0.1388	0.3043	0.5999	0.9815
36	-0.0090	0.0174	0.1558	0.3255	0.6136	0.9703
37	-0.0072	0.0131	0.1338	0.3012	0.6049	0.9912
38	-0.0081	0.0137	0.1370	0.3026	0.6031	0.9758
39	-0.0087	0.0164	0.1472	0.3148	0.6079	0.9596
40	-0.0076	0.0085	0.1153	0.2730	0.5627	0.9116
41	-0.0082	0.0095	0.1189	0.2766	0.5623	0.8978
42	-0.0083	0.0115	0.1271	0.2909	0.5672	0.8919
43	-0.0087	0.0340	0.1759	0.3509	0.6258	0.9597
44	0.0093	0.0630	0.1957	0.3101	0.4475	0.5846
45	0.0031	0.0069	-0.0002	-0.0017	0.0026	0.0053
46	0.0175	0.0548	0.1644	0.2358	0.3256	0.4013
47	0.1330	0.1186	0.1464	0.1605	0.1810	0.1962
48	0.1291	0.1195	0.1311	0.1482	0.1373	0.1458
49	1.8603	0.5372	0.1324	0.0491	0.0042	0.0001
50	0.1624	0.0059	-0.0023	0.0007	0.0038	0.0052
52	0.1200	0.1643	0.1411	0.1477	0.1599	0.1816
53	0.1912	0.0894	0.0113	-0.0006	-0.0019	0.0022
54	0.0993	0.0024	-0.0011	0.0011	0.0035	0.0056
55	-0.0076	-0.0044	-0.0032	-0.0041	0.0050	0.0209
56	0.1042	0.1038	0.1365	0.1595	0.1672	0.1472
57	0.1049	0.1332	0.1322	0.1486	0.1695	0.1831
59	0.0397	-0.0025	-0.0000	0.0036	0.0063	0.0071
60	-0.0014	-0.0025	0.0009	0.0007	0.0022	0.0031

TABLE IV.- PRESSURE COEFFICIENTS FOR $\delta_e = 0^\circ$ AND $R = 1.5 \times 10^6$ - Concluded

Orifice	C_p at α =									
	0°				30°				60°	
	$\beta = 10^\circ$	5°	-5°	-10°	10°	5°	-5°	-10°	-5°	-10°
1	1.8057	1.8671	1.8581	1.8210	1.3540	1.3977	1.3895	1.3724	0.3905	0.3900
2	0.4135	0.4222	0.4198	0.4134	1.3635	1.4069	1.3987	1.3762	1.8686	1.8416
3	0.2074	0.2003	0.1900	0.1902	0.0219	0.0206	0.0226	0.0196	0.0048	0.0036
4	0.2259	0.2258	0.2237	0.2222	1.0716	1.1197	1.1094	1.0912	1.8349	1.8178
5	0.4746	0.3414	0.1613	0.1110	0.8186	0.6840	0.4237	0.3216	0.4998	0.4059
6	0.3628	0.2564	0.1084	0.0691	0.3997	0.2977	0.1502	0.1013	0.1504	0.1137
7	0.2790	0.1901	0.0894	0.0639	0.1896	0.1323	0.0581	0.0359	0.0540	0.0371
8	0.0682	0.0687	0.0685	0.0705	0.0102	0.0146	0.0151	0.0112	0.0046	0.0034
9	0.0957	0.0958	0.0958	0.0971	0.7583	0.8085	0.8133	0.8038	1.6728	1.6574
10	0.3665	0.2548	0.0955	0.0569	0.6909	0.5670	0.3343	0.2452	0.4549	0.3658
11	0.4142	0.2635	0.0841	0.0460	0.4274	0.3004	0.1382	0.0869	0.1434	0.1050
12	0.3653	0.2172	0.0721	0.0448	0.2500	0.1688	0.0727	0.0434	0.0672	0.0460
13	0.1065	0.0757	0.0493	0.0431	0.0083	0.0031	0.0030	0.0024	0.0007	0.0019
14	0.0386	0.0446	0.0444	0.0378	0.0055	0.0073	0.0074	0.0059	0.0024	0.0014
15	0.0401	0.0394	0.0400	0.0403	0.5291	0.5526	0.5540	0.5514	1.4596	1.4464
16	0.0099	0.0104	0.0110	0.0109	0.3070	0.3170	0.3183	0.3182	1.2055	1.2030
17	0.0120	0.0106	0.0097	0.0079	0.3395	0.3338	0.3097	0.2998	1.1803	1.1549
18	0.1645	0.1108	0.0328	0.0185	0.4789	0.3642	0.1770	0.1177	0.3376	0.2626
19	0.3659	0.2476	0.0593	0.0292	0.3786	0.2606	0.0949	0.0503	0.0958	0.0654
20	0.3976	0.2510	0.0556	0.0336	0.1949	0.1259	0.0488	0.0193	0.0363	0.0184
21	0.0029	0.0037	0.0040	0.0038	0.2332	0.2389	0.2403	0.2425	1.0911	1.0949
22	-0.0001	0.0003	0.0007	0.0005	0.1991	0.2031	0.2043	0.2079	1.0602	1.0675
23	-0.0043	-0.0046	-0.0001	0.0013	0.2703	0.2500	0.1985	0.1774	0.9917	0.9412
24	-0.0024	-0.0018	-0.0015	-0.0017	0.1722	0.1754	0.1763	0.1800	1.0236	1.0294
25	-0.0065	-0.0062	-0.0024	-0.0007	0.2362	0.2166	0.1728	0.1568	0.9756	0.9330
26	-0.0038	-0.0035	-0.0033	-0.0034	0.1496	0.1510	0.1519	0.1560	0.9872	0.9925
27	-0.0025	-0.0026	-0.0018	-0.0010	0.1770	0.1676	0.1485	0.1440	0.9696	0.9509
28	-0.0073	-0.0069	-0.0039	-0.0022	0.2023	0.1844	0.1476	0.1358	0.9442	0.9091
29	-0.0043	-0.0044	-0.0043	-0.0041	0.1417	0.1419	0.1427	0.1479	0.9954	1.0009
30	-0.0066	-0.0074	-0.0048	-0.0031	0.1890	0.1716	0.1372	0.1274	0.9595	0.9281
31	-0.0063	-0.0051	-0.0057	-0.0050	0.1395	0.1377	0.1380	0.1443	1.0066	1.0091
32	-0.0040	-0.0039	-0.0041	-0.0035	0.1358	0.1332	0.1334	0.1401	1.0032	1.0057
33	-0.0041	-0.0050	-0.0050	-0.0040	-0.0050	-0.0060	-0.0060	-0.0045	0.0027	0.0029
34	-0.0073	-0.0060	-0.0085	-0.0071	0.1211	0.1246	0.1365	0.1483	1.0070	1.0223
35	-0.0053	-0.0062	-0.0079	-0.0064	0.1111	0.1215	0.1502	0.1711	1.0051	1.0349
36	-0.0065	-0.0075	-0.0085	-0.0077	0.1070	0.1266	0.1766	0.2054	1.0200	1.0779
37	-0.0050	-0.0058	-0.0076	-0.0063	0.1166	0.1215	0.1355	0.1485	1.0043	1.0204
38	-0.0045	-0.0060	-0.0074	-0.0059	0.1072	0.1186	0.1466	0.1675	1.0027	1.0326
39	-0.0063	-0.0074	-0.0078	-0.0067	0.1032	0.1203	0.1672	0.1948	1.0086	1.0578
40	-0.0045	-0.0050	-0.0074	-0.0058	0.1000	0.1054	0.1206	0.1342	0.9258	0.9408
41	-0.0039	-0.0055	-0.0073	-0.0058	0.0931	0.1030	0.1319	0.1524	0.9277	0.9597
42	-0.0057	-0.0066	-0.0073	-0.0060	0.0888	0.1047	0.1521	0.1786	0.9431	0.9959
43	0.0017	-0.0023	-0.0040	-0.0028	0.1231	0.1449	0.1804	0.2270	1.0199	1.0862
44	-0.0080	-0.0010	0.0186	0.0419	0.0859	0.1331	0.2841	0.3988	0.7259	0.8777
45	0.0262	0.0298	0.1122	0.1558	-0.0024	-0.0036	0.0059	0.0161	0.0043	0.0026
46	-0.0063	0.0027	0.0351	0.0618	0.0534	0.0983	0.2688	0.3994	0.5219	0.6622
47	0.0142	0.0639	0.1816	0.2834	0.0456	0.0877	0.2554	0.4087	0.2812	0.3805
48	0.0179	0.0660	0.1503	0.2383	0.0515	0.0962	0.2582	0.4188	0.1999	0.2663
49	0.4107	1.2797	0.5149	0.6305	0.0362	0.0837	0.2364	0.3559	0.0007	0.0034
50	0.0216	0.0643	0.1730	0.1476	-0.0065	-0.0037	-0.0033	-0.0017	0.0054	0.0066
52	0.0414	0.1169	0.2085	0.3153	0.0470	0.0836	0.2641	0.4332	0.2457	0.3242
53	0.1863	0.3043	0.2212	0.2374	-0.0038	0.0026	0.0304	0.0487	0.0027	0.0035
54	0.0323	0.0636	0.0706	0.0649	-0.0052	-0.0018	-0.0049	-0.0053	0.0063	0.0082
55	-0.0052	-0.0056	-0.0071	-0.0061	-0.0032	-0.0053	-0.0069	-0.0071	0.0219	0.0222
56	0.0124	0.0503	0.1252	0.2261	0.0325	0.0741	0.2575	0.3935	0.2396	0.3680
57	0.0265	0.0808	0.1845	0.3264	0.0388	0.0743	0.2568	0.4058	0.2632	0.3591
59	0.0136	0.0294	0.0331	0.0316	-0.0030	0.0026	-0.0000	-0.0012	0.0069	0.0081
60	0.0039	0.0001	-0.0001	0.0012	-0.0022	-0.0013	-0.0018	-0.0026	0.0032	0.0044

TABLE V.- PRESSURE COEFFICIENTS FOR $\delta_e = 15^\circ$ AND $R = 2.1 \times 10^6$

Orifice	C_p at α =			
	30°	40°	50°	60°
	$\beta = 0^\circ$			
1	1.3221	0.9931	0.6548	0.3881
2	1.3627	1.5916	1.7927	1.8268
3	0.0187	0.0080	0.0067	0.0050
4	1.0909	1.3868	1.6613	1.8106
5	0.5335	0.5944	0.6292	0.6131
6	0.2047	0.2116	0.2102	0.1948
7	0.0845	0.0826	0.0809	0.0754
8	0.0172	0.0127	0.0083	0.0037
9	0.7744	1.1012	1.4380	1.6713
10	0.4234	0.5027	0.5511	0.5613
11	0.1966	0.1988	0.1962	0.1864
12	0.1060	0.1066	0.1025	0.0924
13	-0.0011	-0.0035	0.0036	-0.0031
14	0.0090	0.0042	0.0028	0.0023
15	0.5406	0.8213	1.1715	1.4693
16	0.3107	0.5588	0.8797	1.2193
17	0.3136	0.5626	0.8797	1.2201
18	0.2469	0.3172	0.3829	0.4274
19	0.1551	0.1476	0.1433	0.1353
20	0.0743	0.0686	0.0635	0.0536
21	0.2321	0.4494	0.7487	1.1101
22	0.1957	0.3947	0.6929	1.0516
23	0.2186	0.4266	0.7186	1.0712
24	0.1744	0.3651	0.6670	1.0270
25	0.1885	0.3871	0.6805	1.0484
26	0.1491	0.3306	0.6292	1.0186
27	0.1523	0.3338	0.6322	1.0179
28	0.1595	0.3455	0.6372	1.0204
29	0.1485	0.3454	0.6887	1.0848
30	0.1548	0.3502	0.7057	1.1200
31	0.1735	0.3774	0.7100	1.1205
32	0.1592	0.3439	0.6770	1.2196
33	-0.0078	-0.0052	0.0052	0.0079
34	0.1698	0.3725	0.7341	1.3002
35	0.1790	0.3888	0.7330	1.3414
36	0.1987	0.4294	0.7203	1.1462
37	0.2184	0.5093	1.0895	1.4053
38	0.3145	0.6806	1.2686	1.6319
39				
40	0.2824	0.6357	1.1270	1.2855
41	0.3687	0.7483	1.2342	1.4138
42	0.3933	0.7335	1.1600	1.3636
43	0.1711	0.3576	0.6332	0.9872
44	0.1937	0.3103	0.4561	0.5913
45	-0.0012	-0.0046	0.0003	0.0006
46	0.1615	0.2342	0.3318	0.3925
47	0.1443	0.1571	0.1849	0.1924
48				
49	0.1274	0.0418	0.0036	-0.0031
50	-0.0067	-0.0019	0.0018	0.0015
52	0.1389	0.1443	0.1606	0.1901
53	0.0109	-0.0018	-0.0015	-0.0014
54	-0.0053	-0.0015	0.0025	0.0012
55			0.0058	0.0113
56	0.1362	0.1572	0.1653	0.1281
57	0.1318	0.1462	0.1688	0.1811
59	-0.0039	0.0009	0.0021	0.0011
60	-0.0044	-0.0014	0.0005	0.0003

TABLE VI.- PRESSURE COEFFICIENTS FOR $\delta_e = 15^o$ AND $R = 1.5 \times 10^6$

Orifice	C_p at α =			
	30^o	40^o	50^o	60^o
	$\beta = 0^o$			
1	1.3456	1.0171	0.7695	0.3934
2	1.3817	1.6475	1.8217	1.8723
3	0.0181	0.0095	0.0079	0.0061
4	1.0991	1.4347	1.6878	1.8390
5	0.5299	0.5991	0.6289	0.6145
6	0.2083	0.2162	0.2115	0.1982
7	0.0871	0.0844	0.0821	0.0766
8	0.0179	0.0121	0.0089	0.0041
9	0.7805	1.1351	1.4471	1.7000
10	0.4253	0.5069	0.5513	0.5607
11	0.2001	0.2086	0.2025	0.1939
12	0.1085	0.1118	0.1062	0.0964
13	-0.0004	-0.0028	-0.0021	-0.0023
14	0.0092	0.0049	0.0033	0.0032
15	0.5421	0.8566	1.1876	1.4831
16	0.3104	0.5651	0.8818	1.2280
17	0.3148	0.5711	0.8810	1.2271
18	0.2514	0.3838	0.3898	0.4326
19	0.1573	0.1538	0.1477	0.1403
20	0.0755	0.0717	0.0650	0.0566
21	0.2334	0.4553	0.7509	1.1045
22	0.1965	0.3996	0.6961	1.0612
23	0.2192	0.4312	0.7154	1.0601
24	0.1747	0.3709	0.6695	1.0393
25	0.1899	0.3930	0.6808	1.0440
26	0.1506	0.3359	0.6322	1.0286
27	0.1542	0.3435	0.6364	1.0462
28	0.1620	0.3522	0.6394	1.0298
29	0.1502	0.3522	0.6922	1.1049
30	0.1574	0.3594	0.7154	1.1314
31	0.1752	0.3954	0.7359	1.1509
32	0.1640	0.3568	0.6781	1.1852
33	-0.0079	-0.0047	0.0055	0.0123
34	0.1716	0.3837	0.7391	1.2931
35	0.1866	0.3905	0.7417	1.3092
36	0.2012	0.4271	0.7186	1.1219
37	0.2131	0.4934	1.0028	1.5430
38	0.2985	0.6592	1.2400	1.6730
39				
40	0.2701	0.6160	1.1296	1.3787
41	0.3581	0.7365	1.2571	1.4572
42	0.3902	0.7305	1.1638	1.3649
43	0.1725	0.3628	0.6340	0.9894
44	0.1942	0.3183	0.4550	0.5963
45	-0.0011	-0.0044	0.0009	0.0008
46	0.1627	0.2406	0.3346	0.3961
47	0.1455	0.1705	0.1865	0.1947
48				
49	0.1320	0.0457	0.0048	-0.0029
50	-0.0076	-0.0021	0.0019	0.0018
52	0.1410	0.1471	0.1615	0.1875
53	0.0117	-0.0008	-0.0012	-0.0006
54	-0.0064	-0.0016	0.0026	0.0021
55		-0.0002	0.0077	0.0135
56	0.1359	0.1586	0.1640	0.1292
57	0.1323	0.1478	0.1687	0.1809
59	-0.0042	0.0003	0.0021	0.0014
60	-0.0043	-0.0010	0.0007	0.0003

TABLE VII.- PRESSURE COEFFICIENTS FOR $\delta_e = 15^o$ AND $R = 1.1 \times 10^6$

Orifice	C_p at α =	
	30^o	50^o
	$\beta = 0^o$	
1	1.4144	0.6834
2	1.4482	1.8622
3	0.0201	0.0081
4	1.1452	1.7171
5	0.5416	0.6304
6	0.2141	0.2160
7	0.0896	0.0841
8	0.0200	0.0099
9	0.8194	1.4569
10	0.4377	0.5577
11	0.2149	0.2069
12	0.1151	0.1090
13	0.0005	-0.0003
14	0.0100	0.0037
15	0.5613	1.1974
16	0.3220	0.8881
17	0.3296	0.8885
18	0.2567	0.3961
19	0.1655	0.1526
20	0.0791	0.0664
21	0.2402	0.7580
22	0.2013	0.7037
23	0.2283	0.7194
24	0.1784	0.6755
25	0.1971	0.6847
26	0.1540	0.6383
27	0.1610	0.6402
28	0.1668	0.6414
29	0.1514	0.7006
30	0.1612	0.7225
31	0.1830	0.7329
32	0.1726	0.6832
33	-0.0079	0.0053
34	0.1832	0.7229
35	0.2007	0.7419
36	0.2109	0.7228
37	0.2143	0.9437
38	0.2960	1.1805
39		
40	0.2601	1.1029
41	0.3497	1.2533
42	0.3927	1.1683
43	0.1794	0.6395
44	0.2037	0.4572
45	0.0007	0.0011
46	0.1686	0.3378
47	0.1506	0.1886
48		
49	0.1370	0.0058
50	-0.0074	0.0016
52	0.1437	0.1621
53	0.0134	-0.0024
54	-0.0066	0.0019
55		0.0101
56	0.1366	0.1642
57	0.1332	0.1690
59	-0.0043	0.0015
60	-0.0041	0.0004

TABLE VIII.- PRESSURE COEFFICIENTS FOR $\delta_e = 30^o$ AND $R = 2.1 \times 10^6$

Orifice	C_p at α =			
	30^o	40^o	50^o	60^o
	$\beta = 0^o$			
1	1.3196	0.9995	0.6505	0.4022
2	1.3538	1.5993	1.7767	1.8706
3	0.0197	0.0083	0.0066	0.0053
4	1.0820	1.3946	1.6392	1.8857
5	0.5280	0.5953	0.6296	0.6301
6	0.2039	0.2120	0.2110	0.2023
7	0.0845	0.0826	0.0804	0.0792
8	0.0168	0.0108	0.0070	0.0035
9	0.7682	1.1094	1.4182	1.7459
10	0.4219	0.5028	0.5508	0.5898
11	0.1958	0.1996	0.1966	0.1948
12	0.1054	0.1069	0.1031	0.0961
13	-0.0000	-0.0021	-0.0017	-0.0017
14	0.0089	0.0043	0.0028	0.0029
15	0.5350	0.8272	1.1445	1.5152
16	0.3091	0.5588	0.8651	1.2521
17	0.3115	0.5650	0.8740	1.2787
18	0.2461	0.3177	0.3813	0.4495
19	0.1529	0.1473	0.1423	0.1404
20	0.0734	0.0688	0.0619	0.0547
21	0.2319	0.4515	0.7436	1.1337
22	0.1953	0.3988	0.6906	1.0977
23	0.2169	0.4284	0.7134	1.1055
24	0.1734	0.3726	0.7253	1.1204
25	0.1874	0.3866	0.6843	1.0858
26	0.1992	0.4264	0.7650	1.1781
27	0.1826	0.4111	0.7686	1.1809
28	0.1648	0.3773	0.7666	1.1650
29	0.2088	0.4347	0.7701	1.2512
30	0.1994	0.4268	0.7736	1.3159
31	0.2056	0.4364	0.8913	1.4580
32	0.1544	0.3478	0.8644	1.3143
33	-0.0063	-0.0024	0.0011	0.0031
34	0.1840	0.3924	0.9578	1.4714
35	0.1996	0.4198	0.9977	1.5469
36	0.2075	0.4122	0.9247	1.4593
37	0.2184	0.5487	1.2009	1.5752
38	0.4827	1.0366	1.5002	1.9223
39				
40	0.5801	1.2231	1.2911	1.5343
41	0.9254	1.5259	1.6628	1.9275
42	0.9608	1.5669	1.9361	2.2232
43	0.1705	0.3743	0.7399	1.1204
44	0.1933	0.3137	0.4936	0.6470
45	-0.0022	-0.0027	0.0009	0.0029
46	0.1629	0.2427	0.3276	0.3670
47	0.1437	0.1625	0.1860	0.2020
48				
49	0.1256	0.0434	-0.0006	-0.0013
50	-0.0065	-0.0010	0.0011	0.0035
52	0.1387	0.1476	0.1705	0.1960
53	0.0102	-0.0016	-0.0016	0.0007
54	-0.0041	-0.0007	0.0011	0.0033
55			0.0087	0.0051
56	0.1352	0.1566	0.1464	0.1106
57	0.1311	0.1475	0.1724	0.1871
59	-0.0030	0.0011	0.0017	0.0036
60	-0.0030	0.0002	0.0008	0.0028

TABLE IX.- PRESSURE COEFFICIENTS FOR $\delta_e = 30^o$ AND $R = 1.5 \times 10^6$

Orifice	C_p at α =					
	0^o	15^o	30^o	40^o	50^o	60^o
	$\beta = 0^o$					
1	1.8239	1.7401	1.3649	1.0286	0.6695	0.3916
2	0.4158	0.9017	1.4192	1.6902	1.8257	1.8759
3	0.1923	0.0663	0.0183	0.0099	0.0065	0.0061
4	0.2230	0.5934	1.1308	1.4655	1.6946	1.8385
5	0.2363	0.3987	0.5427	0.6134	0.6394	0.6274
6	0.1668	0.1914	0.2149	0.2211	0.2160	0.2017
7	0.1298	0.1025	0.0902	0.0865	0.0832	0.0777
8	0.0668	0.0287	0.0165	0.0118	0.0080	0.0040
9	0.0956	0.3583	0.8093	1.1579	1.4663	1.6996
10	0.1615	0.3028	0.4373	0.5193	0.5560	0.5675
11	0.1510	0.1913	0.2061	0.2131	0.2054	0.1911
12	0.1223	0.1134	0.1124	0.1140	0.1083	0.0957
13	0.0560	0.0131	0.0016	-0.0002	-0.0006	-0.0013
14	0.0472	0.0208	0.0094	0.0053	0.0035	0.0027
15	0.0402	0.1987	0.5618	0.8733	1.1863	1.4865
16	0.0113	0.0897	0.3258	0.5808	0.8859	1.2227
17	0.0104	0.0914	0.3299	0.5871	0.8945	1.2213
18	0.0653	0.1530	0.2620	0.3297	0.3901	0.4379
19	0.1355	0.1531	0.1631	0.1561	0.1492	0.1396
20	0.1220	0.0890	0.0784	0.0727	0.0654	0.0572
21	0.0041	0.0589	0.2453	0.4689	0.7547	1.1155
22	0.0005	0.0436	0.2076	0.4116	0.7014	1.0794
23	-0.0031	0.0519	0.2304	0.4417	0.7227	1.0618
24	-0.0014	0.0344	0.1849	0.3830	0.7518	1.0952
25	-0.0049	0.0412	0.1995	0.4033	0.7153	1.0685
26	-0.0031	0.0376	0.2162	0.4390	0.7953	1.1659
27	-0.0034	0.0367	0.2025	0.4230	0.8008	1.1673
28	-0.0057	0.0328	0.1816	0.3898	0.7918	1.1732
29	-0.0028	0.0451	0.2269	0.4511	0.7956	1.1944
30	-0.0050	0.0426	0.2180	0.4443	0.7922	1.2302
31	-0.0018	0.0470	0.2257	0.4543	0.8595	1.3927
32	-0.0009	0.0422	0.1651	0.3604	0.8446	1.3018
33	-0.0033	-0.0010	-0.0018	-0.0025	0.0032	0.0046
34	-0.0013	0.0382	0.1982	0.4122	0.9290	1.5068
35	-0.0016	0.0418	0.2145	0.4334	0.9572	1.5513
36	-0.0033	0.0462	0.2172	0.4320	0.8636	1.4195
37	0.0074	0.0447	0.2270	0.5096	1.2379	1.7112
38	-0.0007	0.0801	0.4426	0.9829	1.5880	1.9535
39		0.0678	0.3583			
40	0.0079	0.0662	0.5206	1.2378	1.4465	1.7108
41	-0.0038	0.1867	0.9346	1.5620	1.7361	1.9032
42	-0.0044	0.4030	1.0019	1.5961	1.8976	2.0736
43	0.0032	0.0354	0.1617	0.3872	0.7679	1.1001
44	0.0093	0.0627	0.1981	0.3254	0.5064	0.6348
45	0.0509	0.0065	-0.0003	-0.0022	0.0004	0.0034
46	0.0179	0.0551	0.1677	0.2504	0.3157	0.3571
47	0.1267	0.1163	0.1455	0.1670	0.1818	0.1980
48		0.1171	0.1300			
49	1.7981	0.5109	0.1268	0.0467	-0.0022	-0.0019
50	0.1562	0.0053	-0.0023	0.0004	0.0017	0.0043
52	0.1189	0.1598	0.1404	0.1515	0.1685	0.1917
53	0.1794	0.0859	0.0109	-0.0008	-0.0028	0.0026
54	0.0985	0.0018	-0.0011	0.0008	0.0017	0.0044
55	-0.0069	-0.0054	-0.0012	-0.0038	0.0015	0.0055
56	0.1017	0.1018	0.1356	0.1584	0.1469	0.1124
57	0.1024	0.1300	0.1313	0.1492	0.1751	0.1796
59	0.0383	-0.0029	-0.0001	0.0024	0.0028	0.0048
60	-0.0019	-0.0022	0.0027	0.0018	0.0024	0.0038

TABLE IX.- PRESSURE COEFFICIENTS FOR $\delta_e = 30^\circ$ AND $R = 1.5 \times 10^6$ - Concluded

Orifice	C_p at α =							
	0°				30°			
	$\beta = 10^\circ$	5°	-5°	-10°	$\beta = 10^\circ$	5°	-5°	-10°
1	1.7964	1.8384	1.8474	1.8257	1.3227	1.3622	1.3582	1.3151
2	0.4149	0.4236	0.4217	0.4195	1.3728	1.4009	1.3905	1.3786
3	0.2036	0.1969	0.1894	0.1903	0.0203	0.0265	0.0169	0.0172
4	0.2270	0.2281	0.2252	0.2249	1.1071	1.1211	1.1056	1.1017
5	0.4807	0.3419	0.1611	0.1109	0.8098	0.6661	0.4359	0.3438
6	0.3872	0.2559	0.1072	0.0674	0.3814	0.2860	0.1550	0.1121
7	0.2834	0.1901	0.0896	0.0638	0.1775	0.1270	0.0605	0.0408
8	0.0683	0.0664	0.0679	0.0696	0.0108	0.0143	0.0142	0.0113
9	0.0963	0.0963	0.0967	0.0984	0.7996	0.8034	0.7958	0.7974
10	0.3726	0.2571	0.0969	0.0580	0.6744	0.5442	0.3398	0.2644
11	0.4202	0.2654	0.0853	0.0472	0.3904	0.2874	0.1451	0.0962
12	0.3710	0.2194	0.0723	0.0451	0.2262	0.1619	0.0752	0.0479
13	0.1069	0.0744	0.0491	0.0429	0.0065	0.0026	0.0023	0.0028
14	0.0389	0.0454	0.0450	0.0385	0.0055	0.0072	0.0073	0.0058
15	0.0389	0.0400	0.0431	0.0437	0.5636	0.5599	0.5573	0.5632
16	0.0101	0.0107	0.0113	0.0110	0.3309	0.3249	0.3260	0.3316
17	0.0126	0.0116	0.0105	0.0082	0.3594	0.3410	0.3173	0.3135
18	0.1673	0.1116	0.0337	0.0186	0.4696	0.3550	0.1869	0.1341
19	0.3691	0.2509	0.0603	0.0294	0.3555	0.2485	0.1005	0.0561
20	0.3988	0.2561	0.0561	0.0324	0.1791	0.1212	0.0483	0.0268
21	0.0030	0.0035	0.0043	0.0039	0.2502	0.2451	0.2454	0.2525
22	-0.0001	0.0000	0.0006	0.0005	0.2139	0.2077	0.2081	0.2160
23	-0.0048	-0.0049	0.0002	0.0011	0.2861	0.2557	0.2074	0.1923
24	-0.0023	-0.0018	-0.0014	-0.0017	0.1901	0.1839	0.1849	0.1924
25	-0.0067	-0.0061	-0.0021	-0.0006	0.2500	0.2215	0.1818	0.1709
26	-0.0031	-0.0032	-0.0029	-0.0028	0.1748	0.1934	0.2009	0.1833
27	-0.0046	-0.0043	-0.0010	-0.0002	0.1902	0.1783	0.2084	0.2072
28	-0.0073	-0.0068	-0.0034	-0.0017	0.2136	0.1892	0.2006	0.2035
29	-0.0024	-0.0025	-0.0026	-0.0019	0.2096	0.2144	0.2188	0.2145
30	-0.0065	-0.0061	-0.0032	-0.0006	0.2232	0.2149	0.2164	0.2118
31	-0.0022	-0.0013	-0.0014	-0.0018	0.2028	0.2076	0.2217	0.2181
32	-0.0028	-0.0013	-0.0005	-0.0023	0.1649	0.1621	0.1582	0.1559
33	-0.0038	-0.0051	-0.0049	-0.0041	0.0052	-0.0003	-0.0014	0.0017
34	-0.0019	-0.0019	-0.0033	-0.0044	0.2471	0.2247	0.2037	0.2326
35	0.0034	0.0045	-0.0039	-0.0025	0.2179	0.2147	0.2168	0.2348
36	0.0008	-0.0005	-0.0051	-0.0041	0.1683	0.1862	0.2489	0.2935
37	0.0018	0.0015	-0.0029	-0.0029	0.2447	0.2187	0.3061	0.4500
38	0.0028	0.0126	-0.0037	-0.0026	0.2875	0.2797	0.7287	0.9738
39	0.0098	-	-0.0022	-0.0026	0.2583	0.2618	0.5859	0.8034
40	0.0020	0.0006	-0.0039	-0.0034	0.5389	0.4327	0.7447	0.9286
41	0.0021	0.0124	-0.0048	-0.0038	0.7631	0.7684	1.0916	1.2051
42	0.0108	-0.0014	-0.0048	0.0099	0.8395	0.9097	1.1013	1.3054
43	-0.0002	-0.0022	-0.0038	-0.0035	0.1915	0.1970	0.2054	0.2374
44	-0.0055	-0.0004	0.0205	0.0424	0.1246	0.1446	0.2755	0.3770
45	0.0225	0.0297	0.1095	0.1551	0.0002	-0.0024	0.0040	0.0100
46	-0.0048	0.0032	0.0332	0.0611	0.0467	0.1005	0.2507	0.3661
47	0.0150	0.0618	0.1790	0.2804	0.0513	0.0984	0.2308	0.3573
48	0.0229	0.1168	0.1479	0.2351	0.0520	0.0938	0.1897	0.3010
49	0.3779	1.2291	0.5124	0.6351	0.0315	0.0739	0.1917	0.2716
50	0.0202	0.0603	0.1704	0.1453	-0.0013	-0.0008	-0.0033	-0.0013
52	0.0384	0.1115	0.1880	0.3004	0.0506	0.0892	0.2340	0.3700
53	0.1736	0.2922	0.2190	0.2329	-0.0015	0.0026	0.0273	0.0418
54	0.0319	0.0595	0.0719	0.0640	-0.0007	-0.0004	-0.0005	-0.0000
55	-0.0054	-0.0054	-0.0077	-0.0069	-0.0004	-0.0030	-0.0043	-0.0027
56	0.0118	0.0453	0.1227	0.2218	0.0299	0.0697	0.2311	0.3502
57	0.0224	0.0768	0.1791	0.3211	0.0374	0.0740	0.2249	0.3586
59	0.0126	0.0260	0.0339	0.0329	-0.0002	0.0010	0.0006	0.0011
60	0.0014	-0.0017	0.0003	0.0007	-0.0003	0.0008	0.0012	0.0021

TABLE X.- PRESSURE COEFFICIENTS FOR $\delta_e = 30^o$ AND $R = 1.1 \times 10^6$

Orifice	C_p at α =			
	30^o	40^o	50^o	60^o
	$\beta = 0^o$			
1	1.4269	1.0499	0.6920	0.3998
2	1.4621	1.7218	1.8893	1.9154
3	0.0199	0.0117	0.0090	0.0068
4	1.1575	1.4988	1.7633	1.8906
5	0.5540	0.6241	0.6617	0.6215
6	0.2186	0.2281	0.2263	0.2040
7	0.0909	0.0896	0.0879	0.0796
8	0.0171	0.0131	0.0085	0.0040
9	0.8295	1.1831	1.5201	1.7399
10	0.4458	0.5316	0.5810	0.5728
11	0.2165	0.2188	0.2159	0.1981
12	0.1171	0.1192	0.1152	0.1012
13	0.0032	0.0015	0.0010	0.0011
14	0.0103	0.0057	0.0043	0.0036
15	0.5698	0.8957	1.2401	1.5164
16	0.3261	0.5907	0.9171	1.2492
17	0.3339	0.5968	0.9256	1.2468
18	0.2581	0.3387	0.4071	0.4443
19	0.1663	0.1621	0.1573	0.1459
20	0.0805	0.0758	0.0692	0.0598
21	0.2444	0.4760	0.7836	1.1238
22	0.2049	0.4198	0.7272	1.0889
23	0.2305	0.4494	0.7447	1.0801
24	0.1824	0.3910	0.7887	1.1276
25	0.1986	0.4104	0.7371	1.1020
26	0.2103	0.4489	0.8347	1.1964
27	0.1981	0.4342	0.8291	1.2029
28	0.1787	0.4023	0.8197	1.1872
29	0.2235	0.4661	0.8361	1.2049
30	0.2165	0.4599	0.8217	1.2123
31	0.2333	0.4656	0.8441	1.3556
32	0.1712	0.3643	0.7981	1.2861
33	-0.0072	-0.0029	0.0062	0.0063
34	0.2018	0.4210	0.8420	1.4727
35	0.2188	0.4443	0.8660	1.5346
36	0.2201	0.4408	0.7926	1.4054
37	0.2266	0.5133	1.2155	1.7013
38	0.4127	0.9502	1.6817	1.9979
39				
40	0.4520	1.2426	1.5403	1.7173
41	0.8689	1.6032	1.8701	1.9701
42	1.0017	1.6135	1.9883	2.0548
43	0.1834	0.3928	0.7980	1.1370
44	0.2059	0.3292	0.5214	0.6436
45	0.0013	0.0000	0.0018	0.0044
46	0.1743	0.2546	0.3151	0.3688
47	0.1528	0.1711	0.1849	0.1978
48				
49	0.1378	0.0499	-0.0018	-0.0034
50	-0.0043	0.0015	0.0026	0.0047
52	0.1463	0.1548	0.1634	0.1928
53	0.0131	0.0003	-0.0050	-0.0022
54	-0.0034	0.0017	0.0032	0.0055
55	-0.0073	-0.0036	0.0020	0.0082
56	0.1387	0.1608	0.1530	0.1186
57	0.1353	0.1517	0.1789	0.1822
59	-0.0017	0.0029	0.0032	0.0056
60	-0.0014	0.0030	0.0032	0.0061

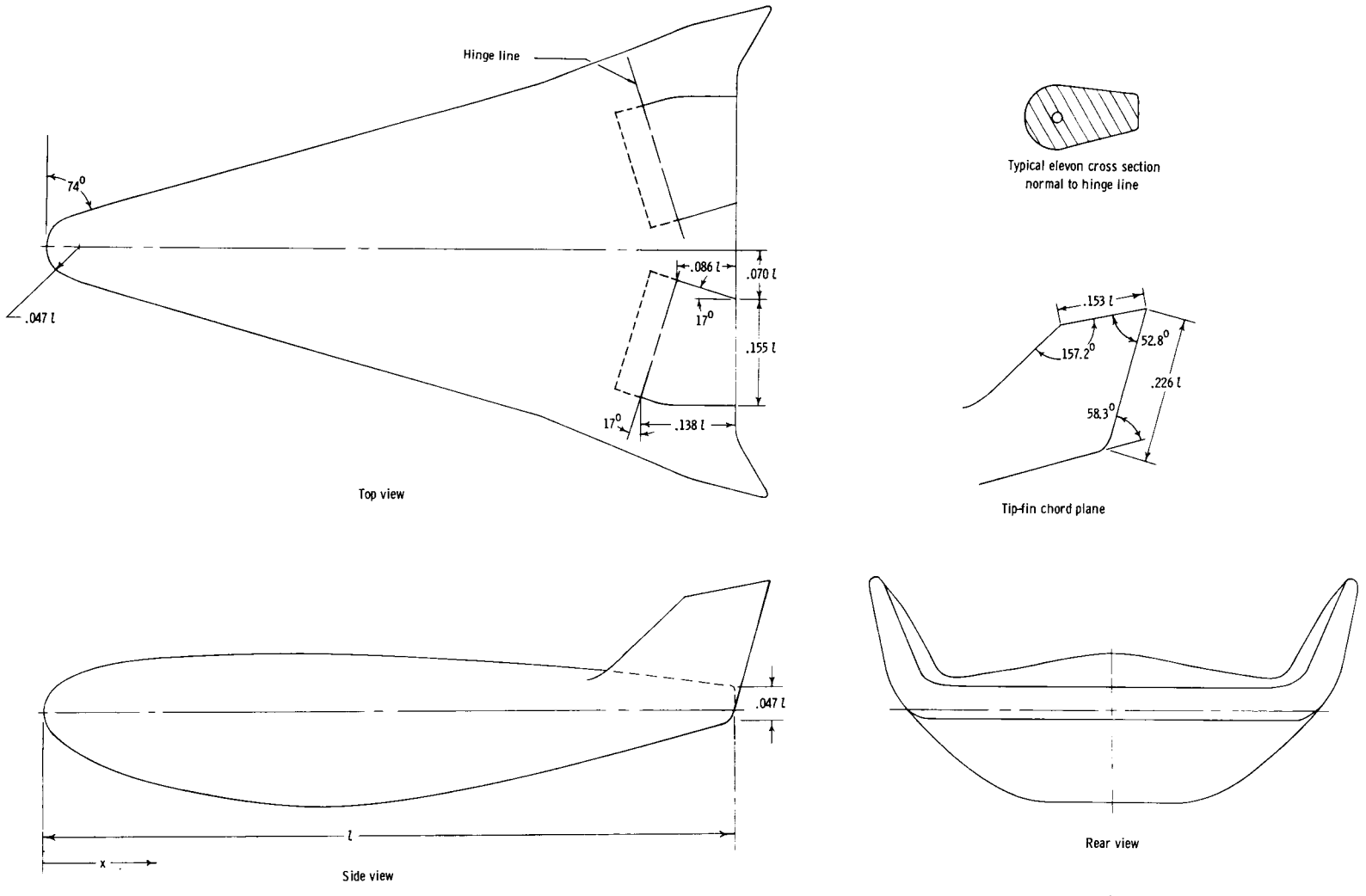

Figure 1.- Three-view drawing showing details of model. l = 12 inches (30.48 cm).

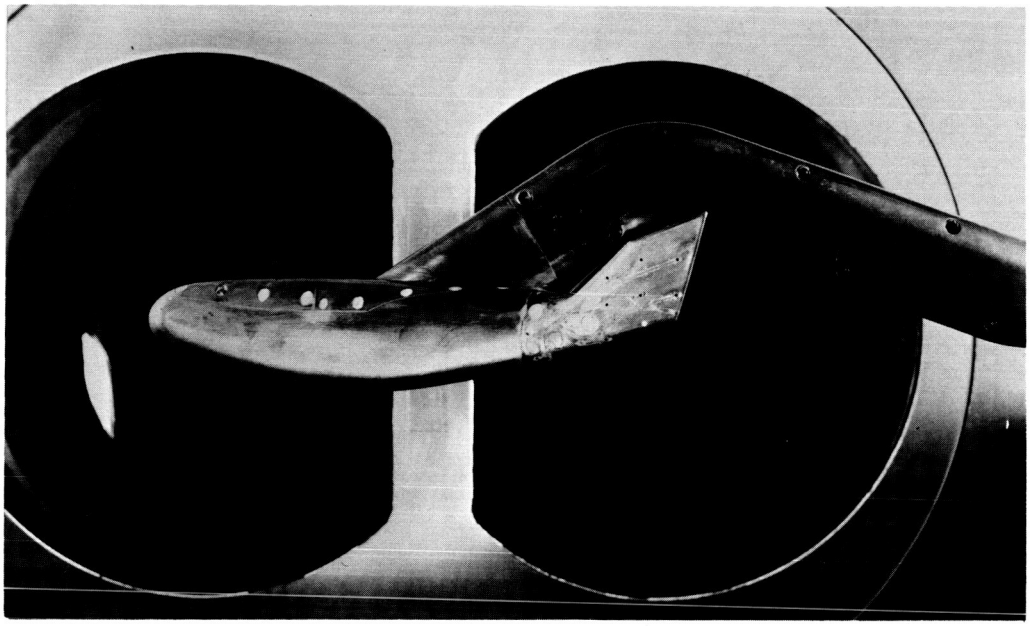

(a) Model and bent sting.

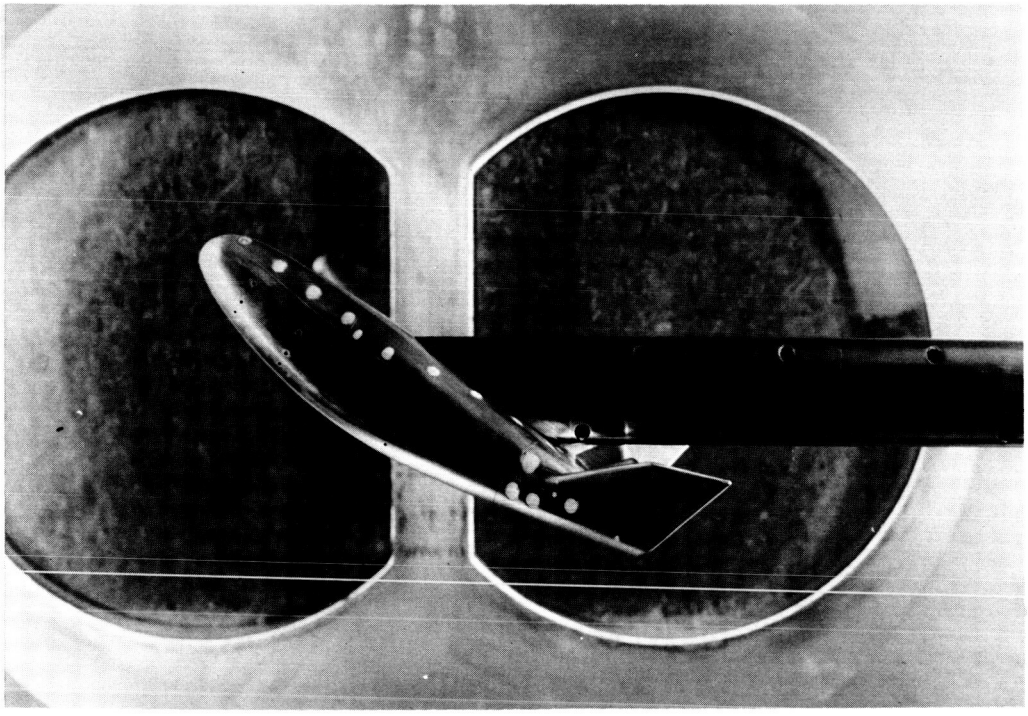

(b) Model and straight sting.

L-68-857

Figure 2.- Photographs of model-sting arrangements.

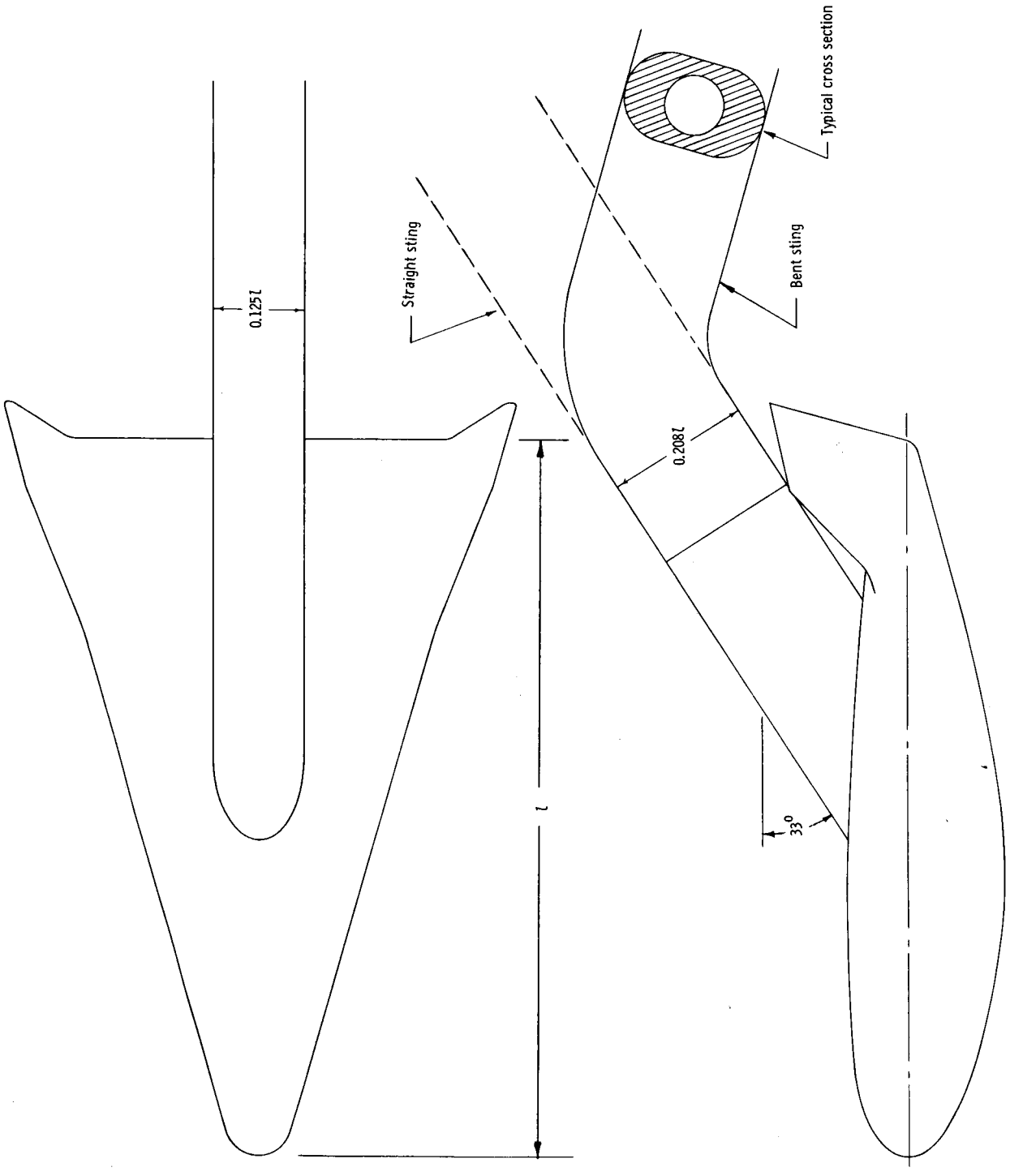

Figure 3.- Drawings of model-sting arrangements.

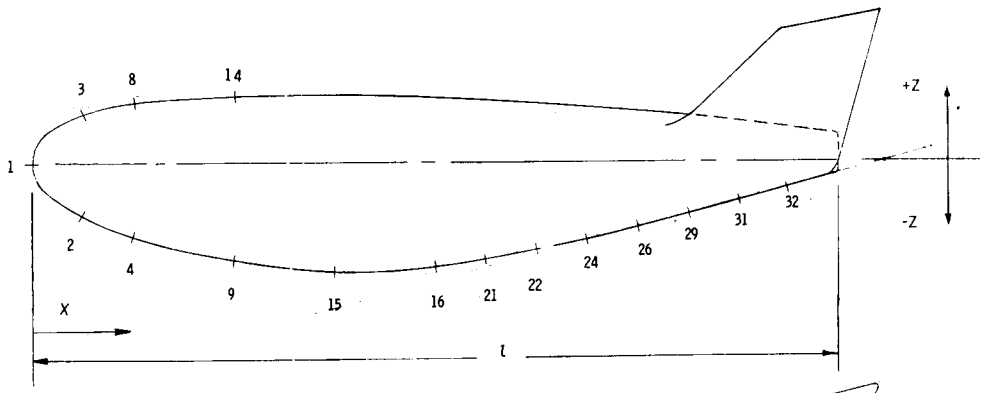

Side view

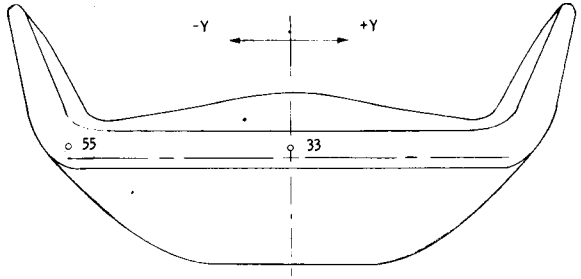

Rear view
(elevons omitted)

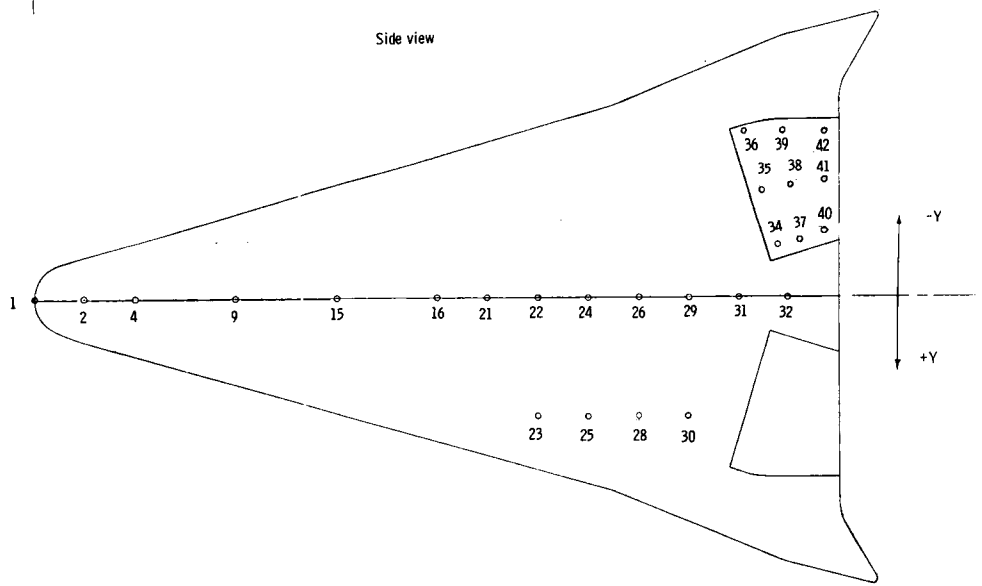

Bottom view

Left elevon

Orifice	x/l	y/l
34	0.925	-0.065
35	.904	.136
36	.882	.210
37	.951	.071
38	.940	.142
39	.929	.209
40	.983	.083
41	.982	.147
42	.982	.209

Outboard row

Orifice	x/l	y/l
23	0.625	0.148
25	.687	.148
28	.750	.148
30	.812	.148

Model base

Orifice	x/l	y/l	z/l
33	1.000	0	0.0111
55	1.004	-.276	.0152

Model centerline

Orifice	x/l
1	0
2	.062
3	.062
4	.125
8	.125
9	.250
14	.250
15	.375
16	.500
21	.562
22	.625
24	.687
26	.750
29	.812
31	.875
32	.938

Figure 4.- Orifice locations on lower surface, elevon, base region, ard upper surface.

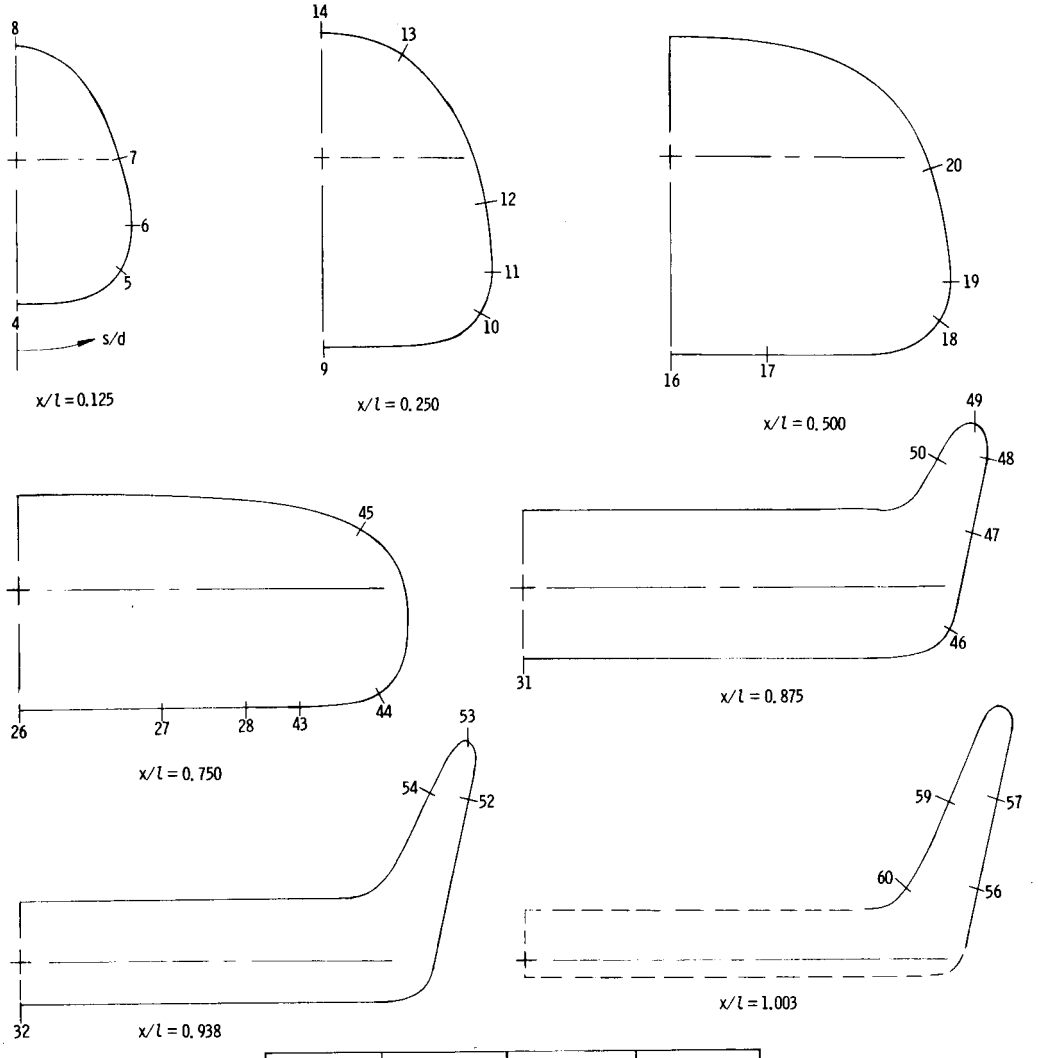

x/l = 0.125		x/l = 0.250		x/l = 0.500		x/l = 0.750	
Orifice	s/d	Orifice	s/d	Orifice	s/d	Orifice	s/d
4	0	9	0	16	0	26	0
5	.791	10	1.176	17	.674	27	1.005
6	1.102	11	1.465	18	1.957	28	1.604
7	1.572	12	1.957	19	2.235	43	-1.979
8	2.952	13	3.155	20	3.059	44	-2.556
		14	3.754			45	-3.872

x/l = 0.875		x/l = 0.938		x/l = 1.003	
Orifice	s/d	Orifice	s/d	Orifice	s/d
31	0	32	0	56	-3.921
46	-3.048	52	-4.597	57	-4.614
47	-3.733	53	-5.069	59	-6.272
48	-4.246	54	-5.583	60	-7.010
49	-4.535				
50	-4.920				

Figure 5.- Orifice locations for seven longitudinal stations. Negative values of s/d indicate left side of model.

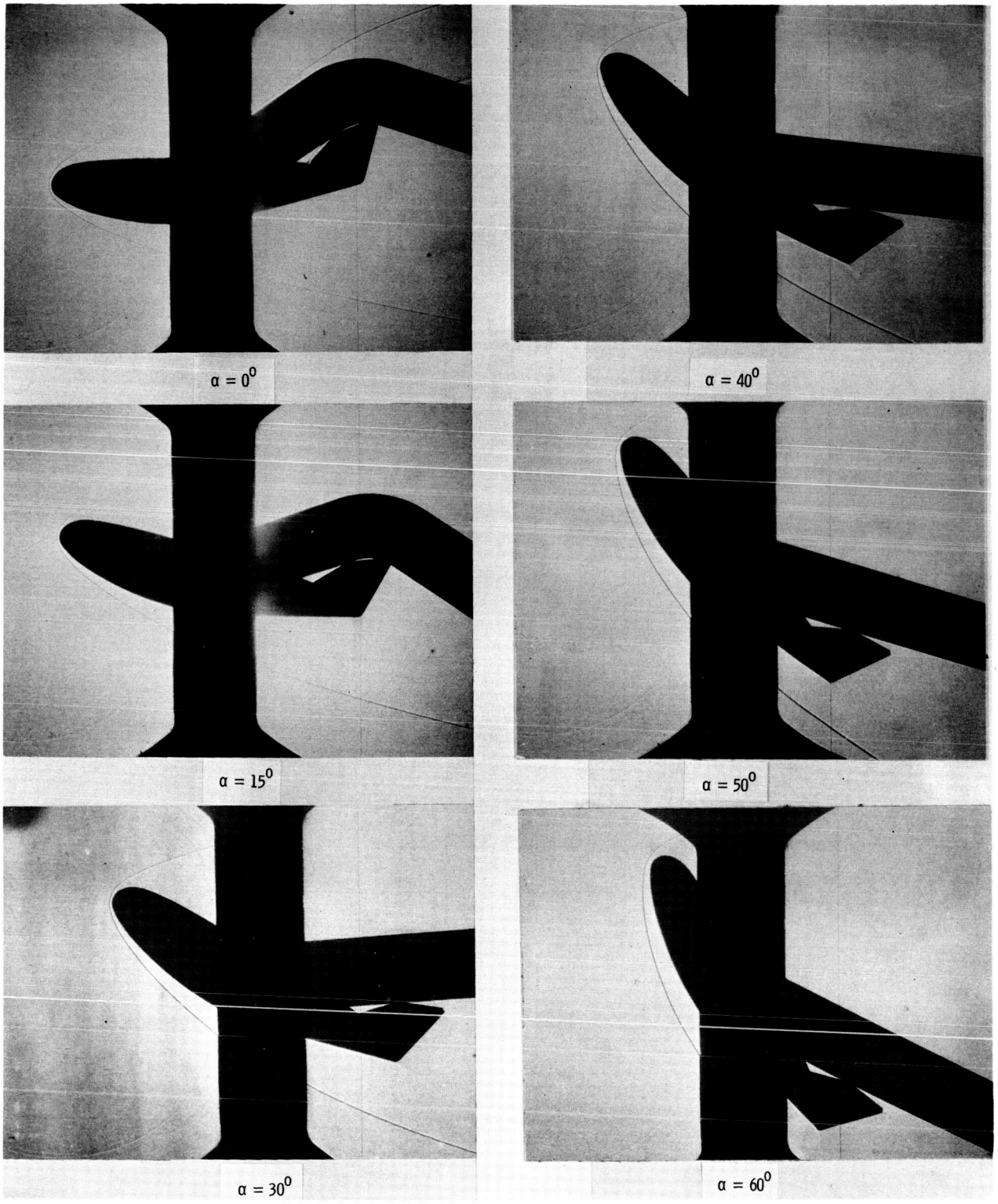

Figure 6.- Shadowgraph pictures of model flow field for various angles of attack at $\delta_e = 0^0$. $R = 2.1 \times 10^6$. L-68-858

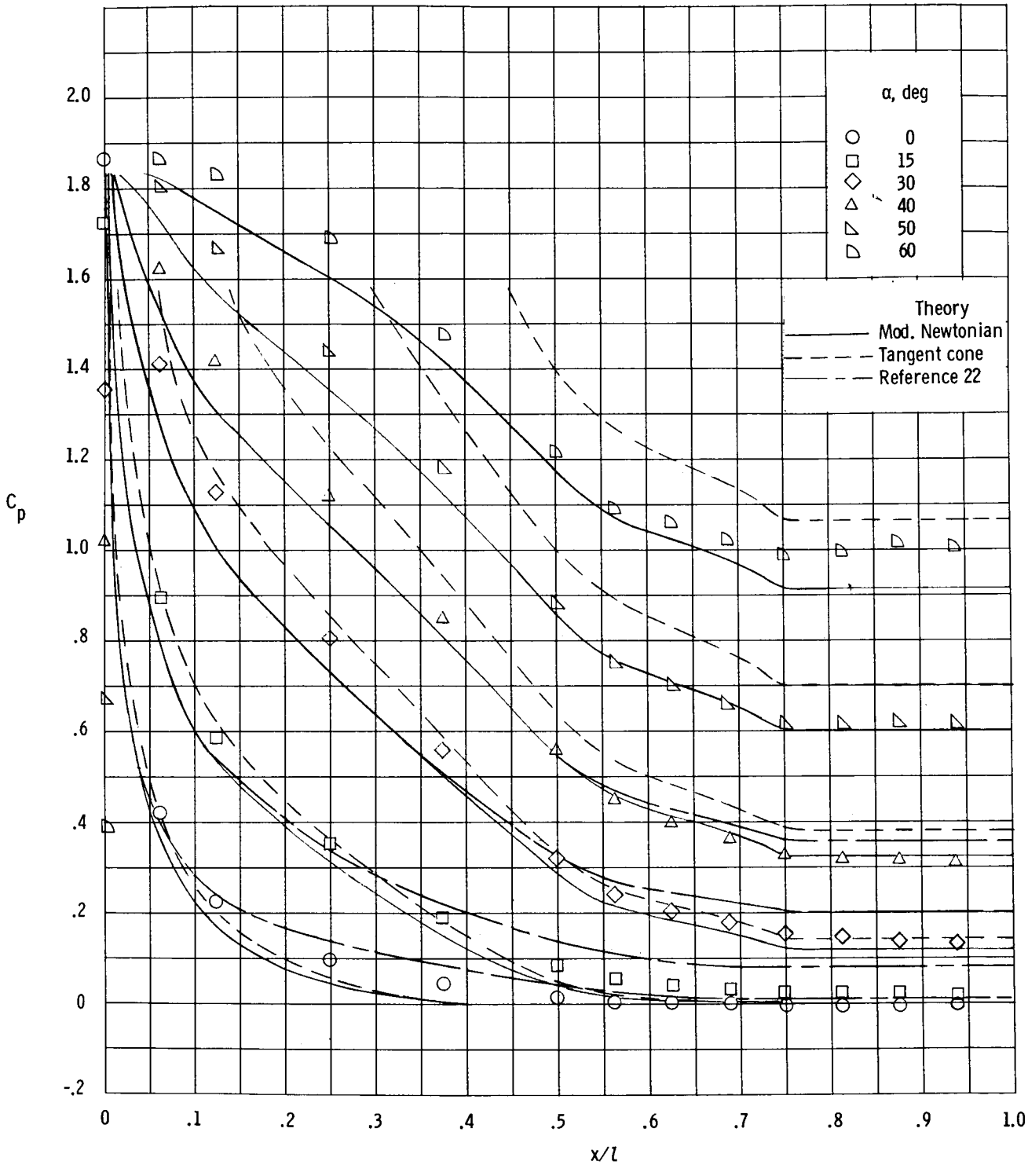

Figure 7.- Comparison of theoretical and experimental pressure distributions on windward center line at $\delta_e = 0^o$. $R = 1.5 \times 10^6$.

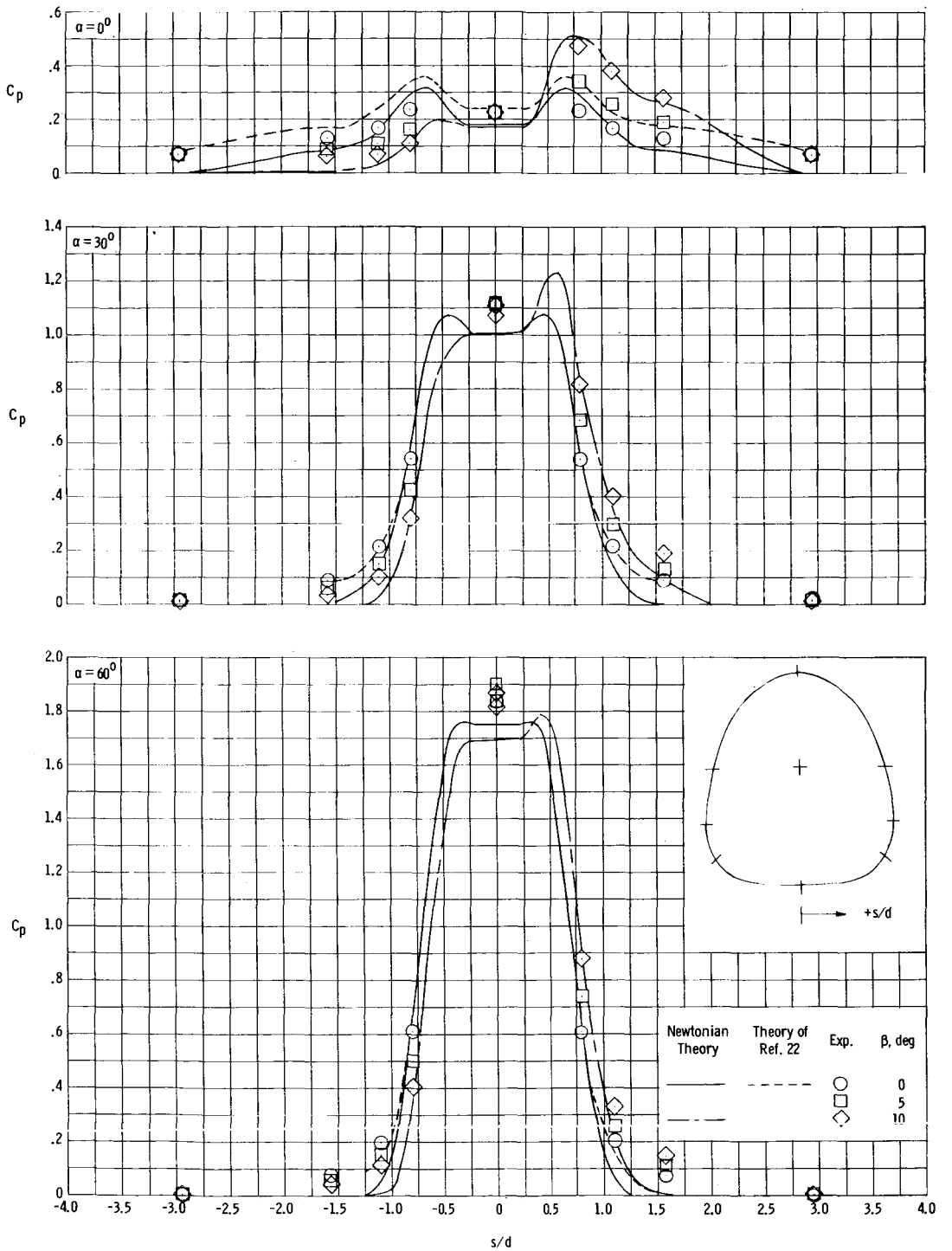

(a) x/l = 0.125.

Figure 8.- Comparison of theoretical and experimental pressure distributions for seven lateral cross sections at $\delta_e = 0^o$. $R = 1.5 \times 10^6$.

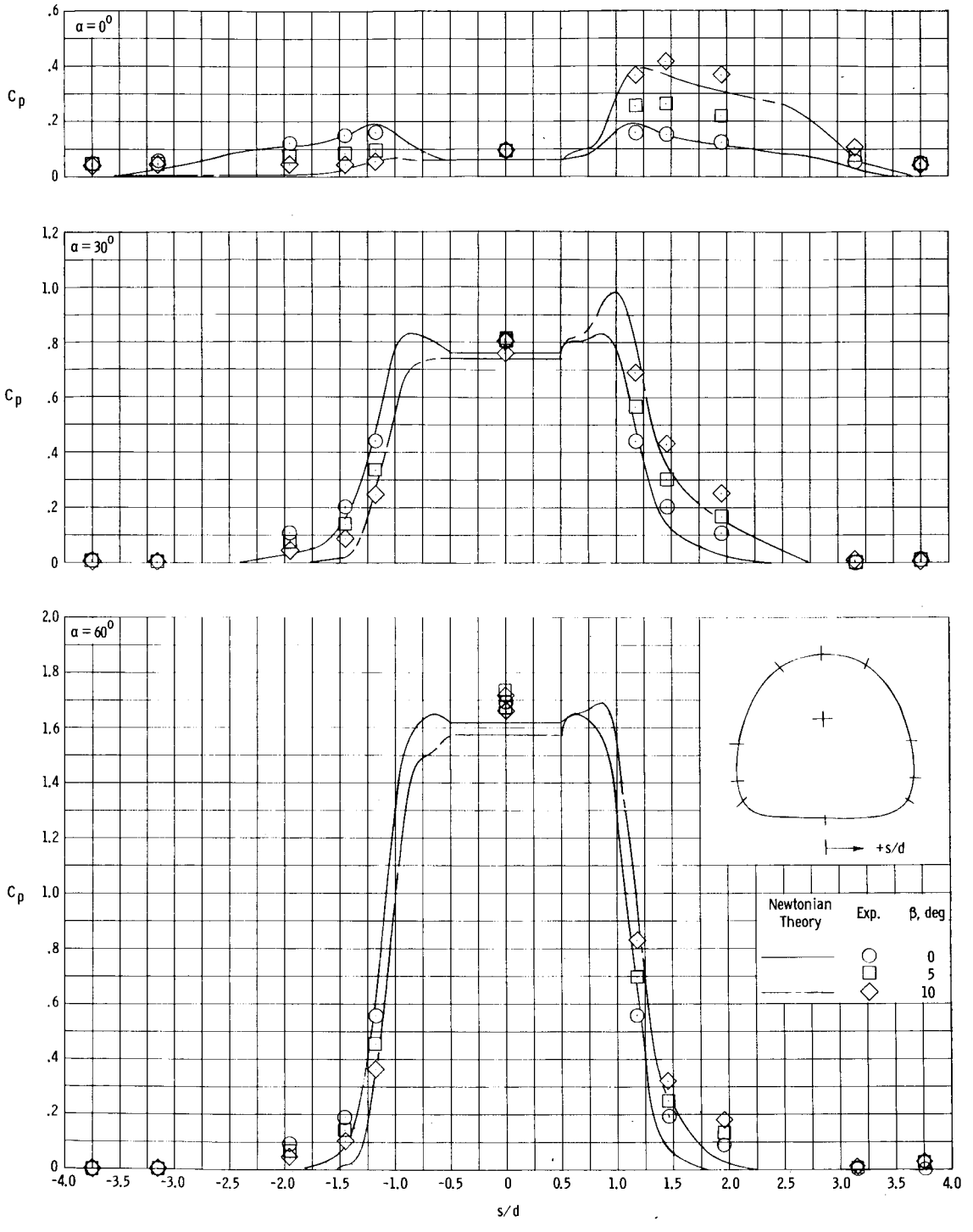

(b) $x/l = 0.250$.

Figure 8.- Continued.

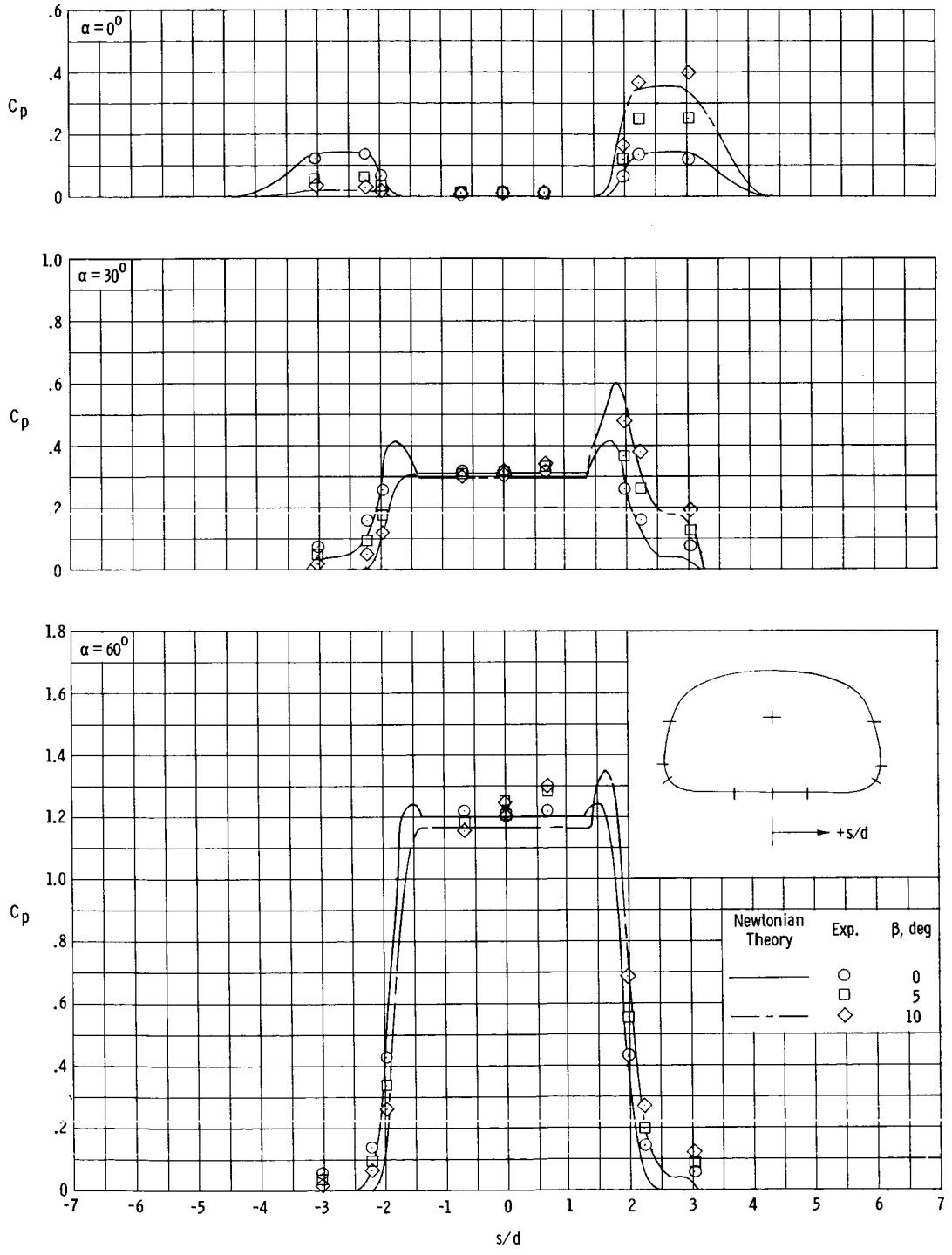

(c) x/l = 0.500.

Figure 8.- Continued.

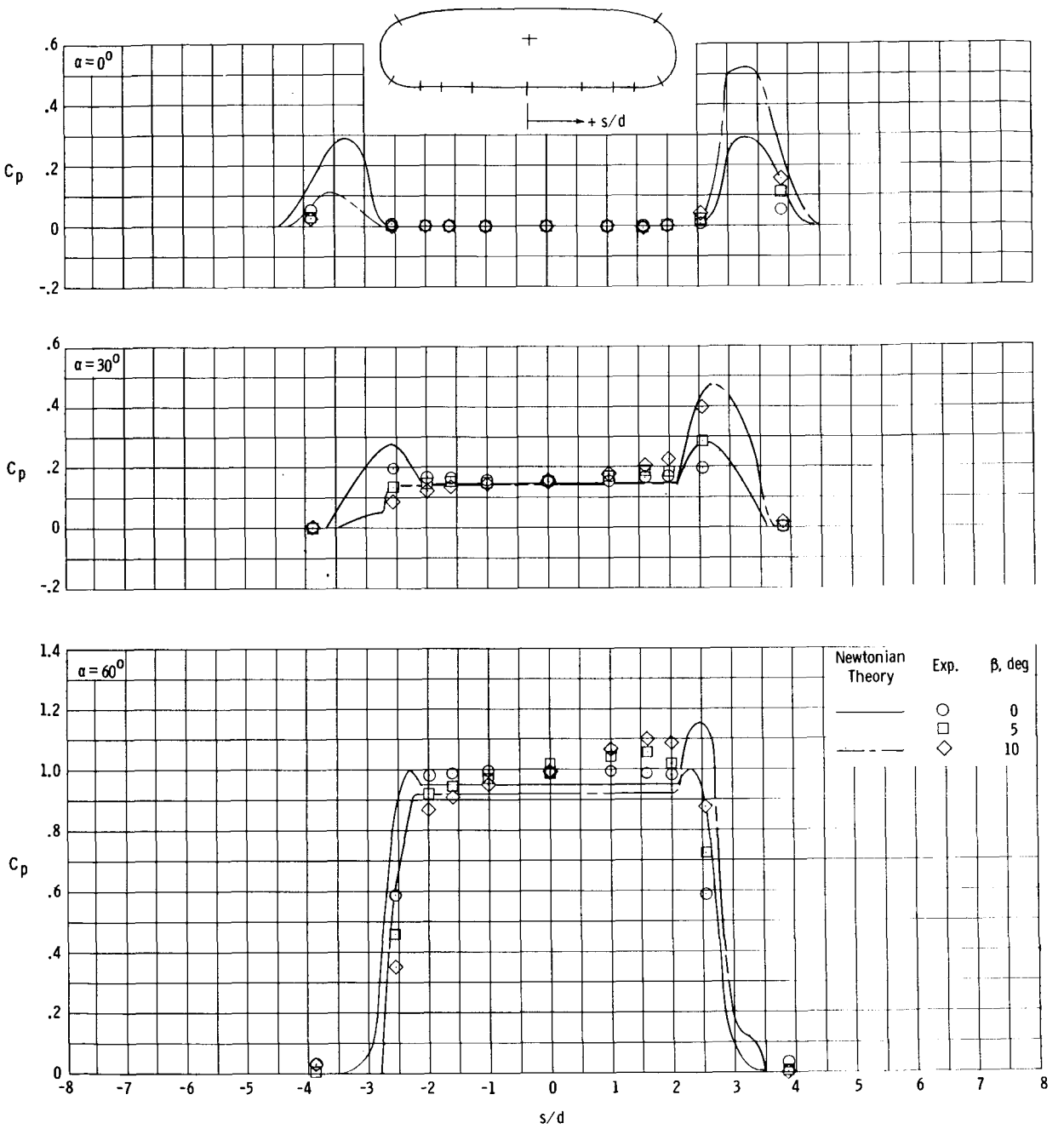

(d) x/l = 0.750.

Figure 8.- Continued.

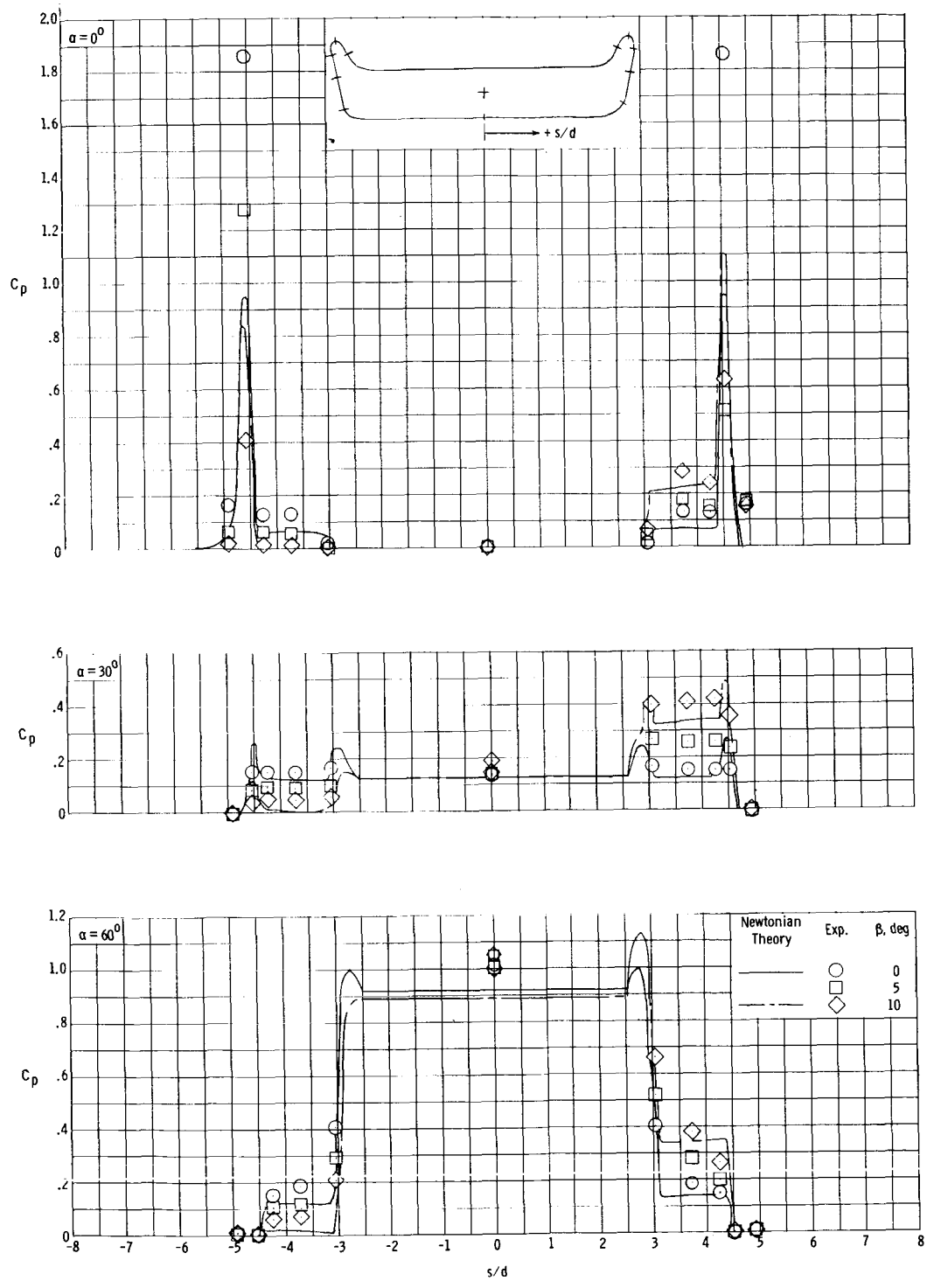

(e) x/l = 0.875.

Figure 8.- Continued.

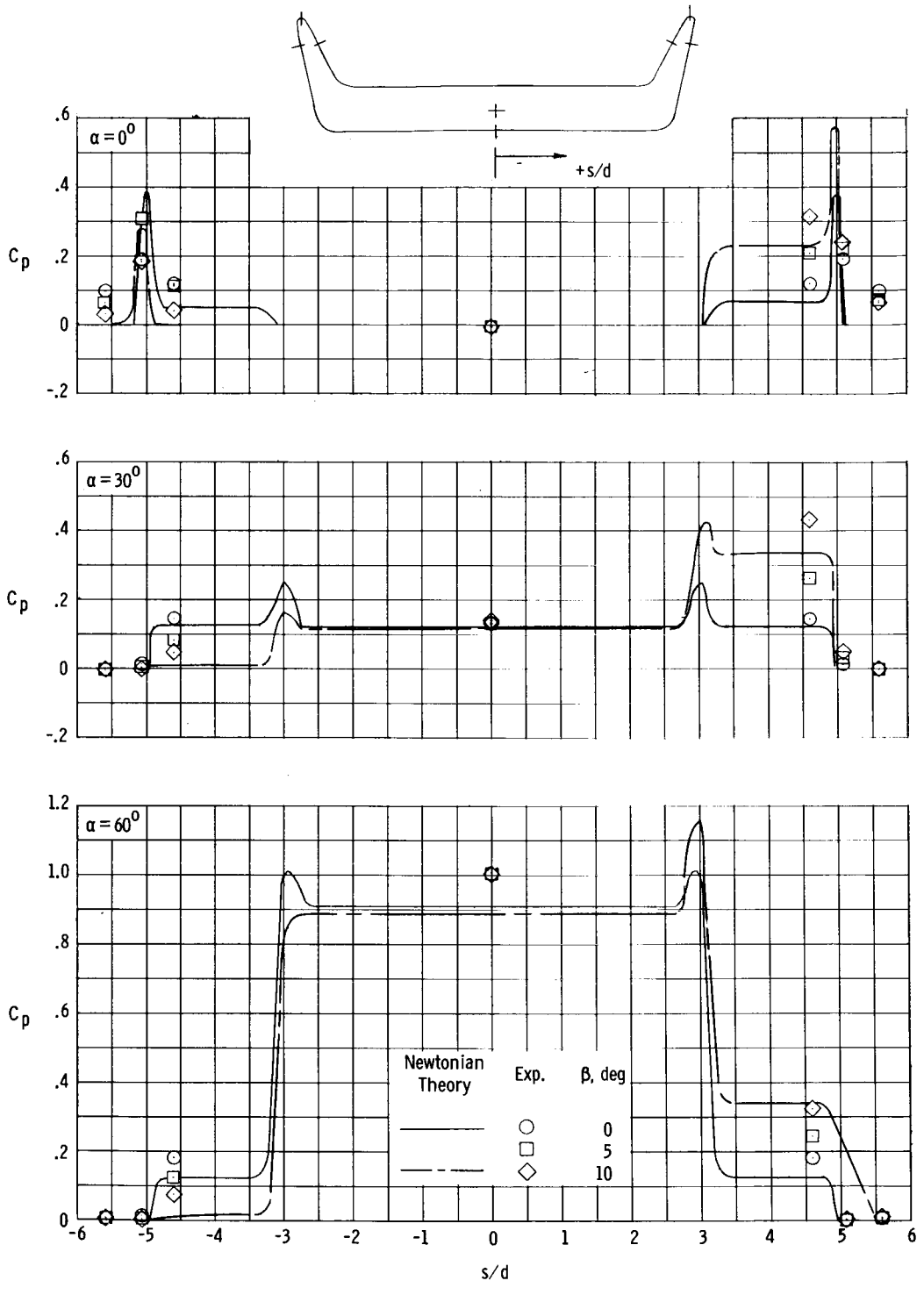

(f) x/l = 0.938.

Figure 8.- Continued.

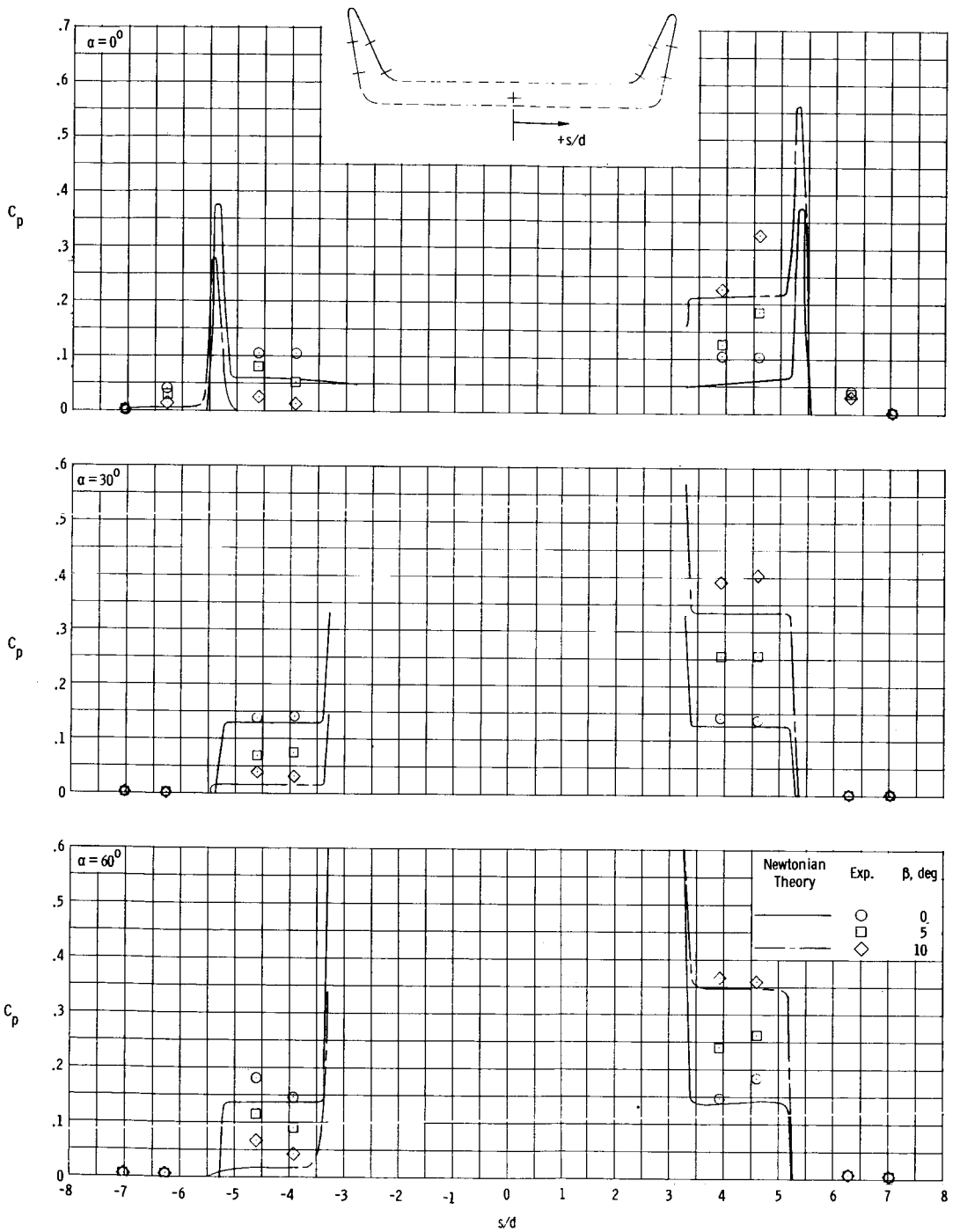

(g) x/l = 1.003.

Figure 8.- Concluded.

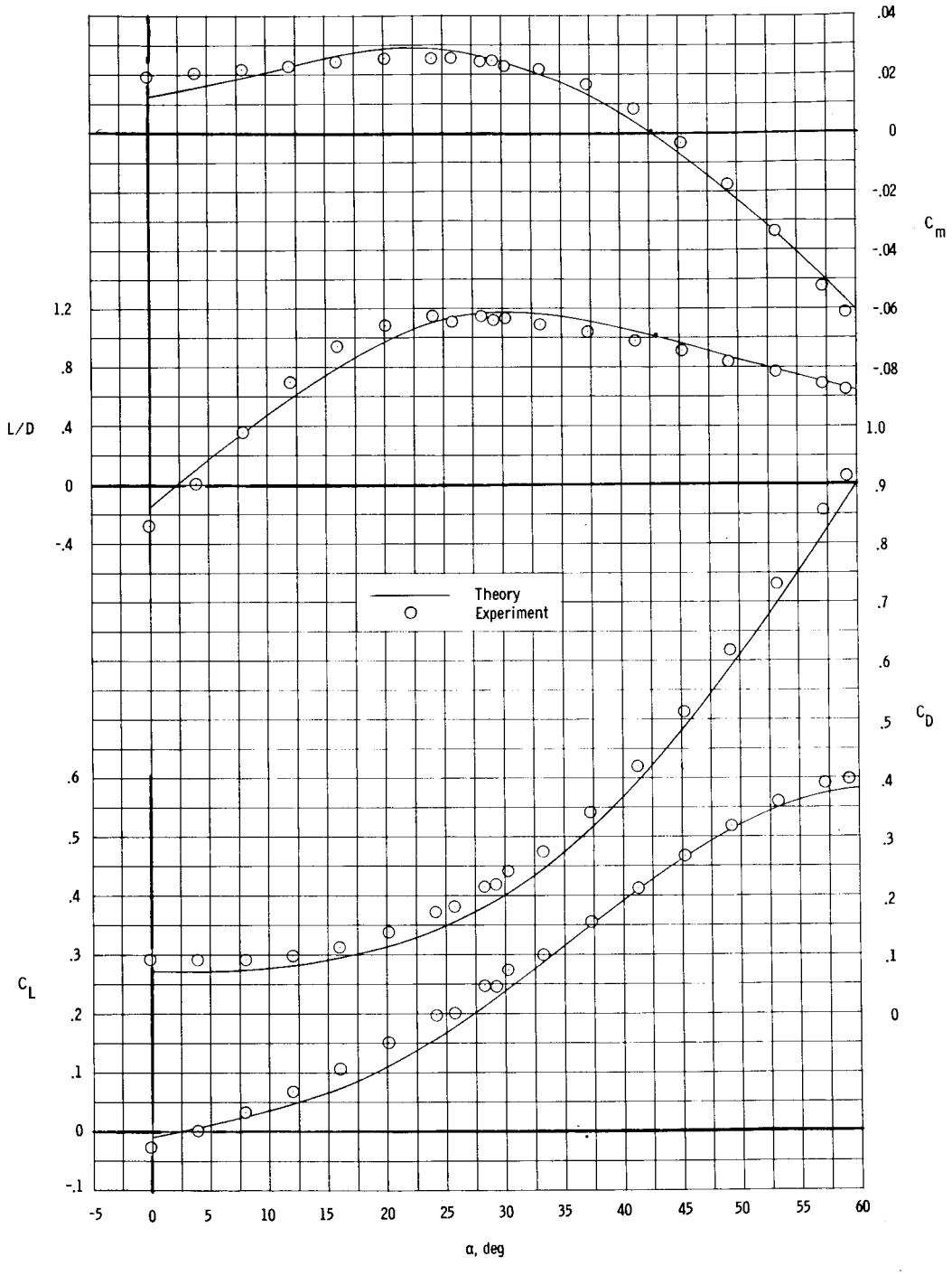

(a) Longitudinal characteristics.

Figure 9.- Comparison of theoretical and experimental force characteristics. (Data from ref. 18.)

$M = 10.5$

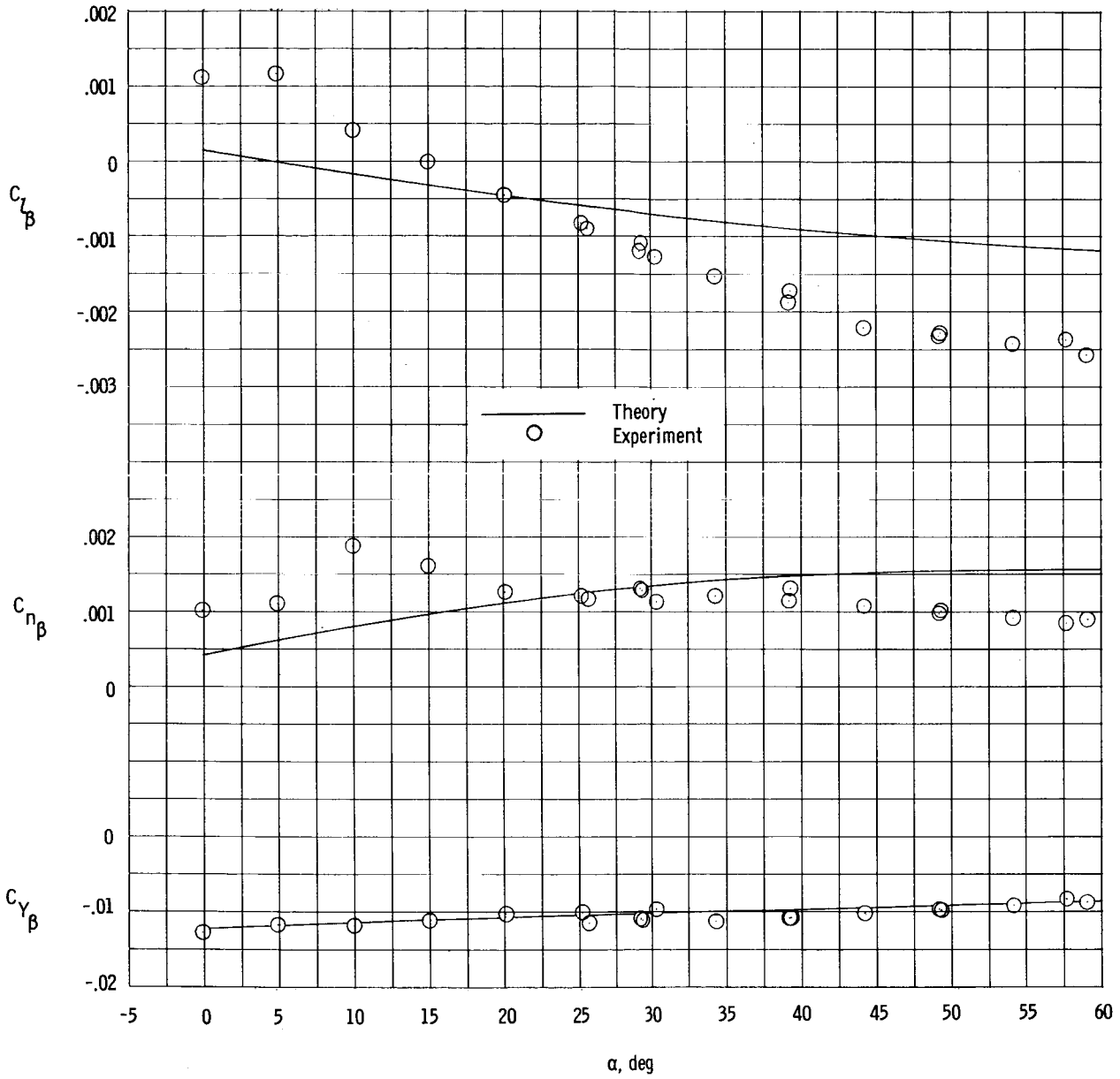

(b) Directional and lateral stability characteristics.

Figure 9.- Concluded.

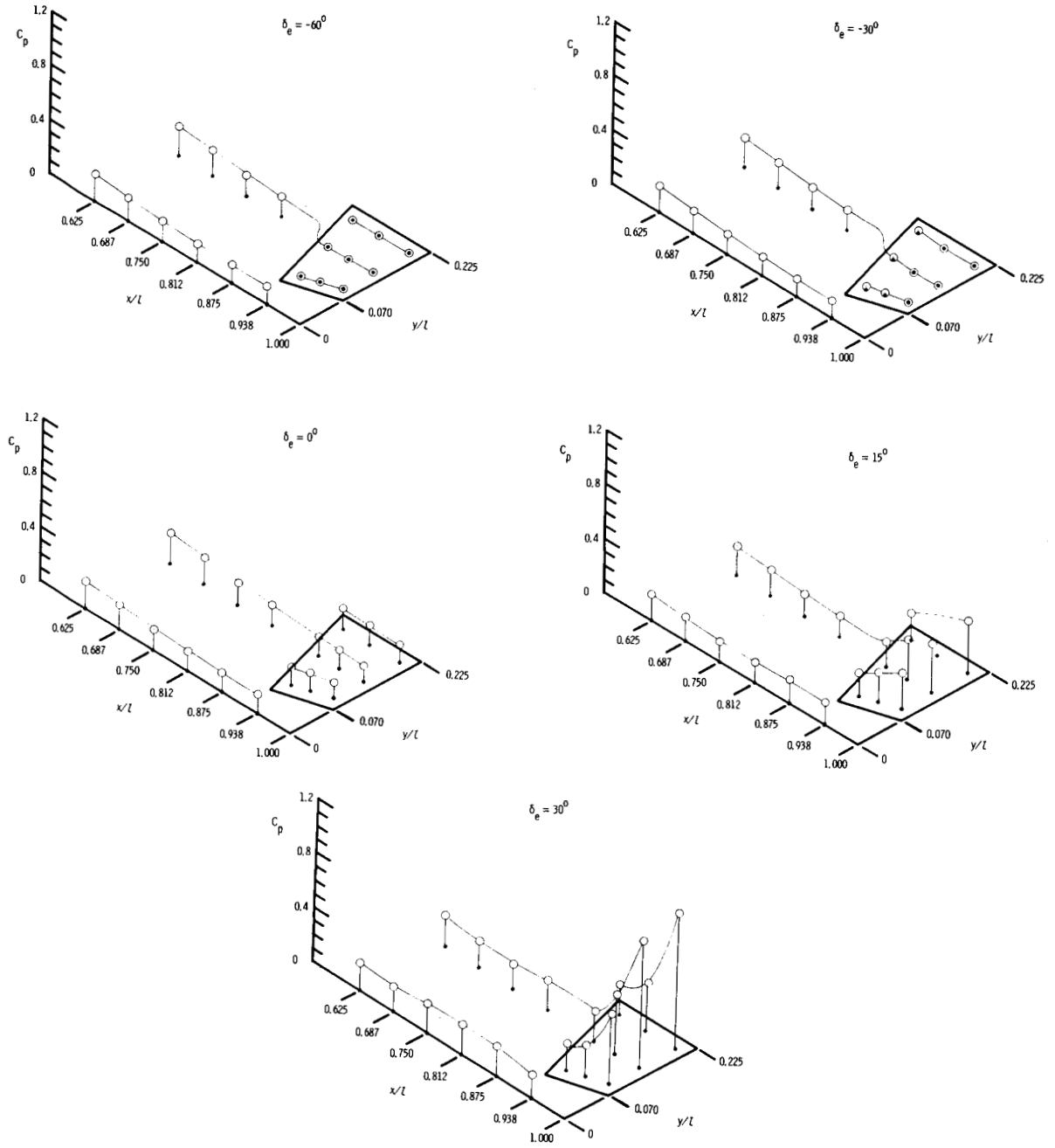

(a) $\alpha = 30^0$.

Figure 10.- Effect of elevon deflection on elevon and adjacent area pressure distributions. $R = 1.5 \times 10^6$.

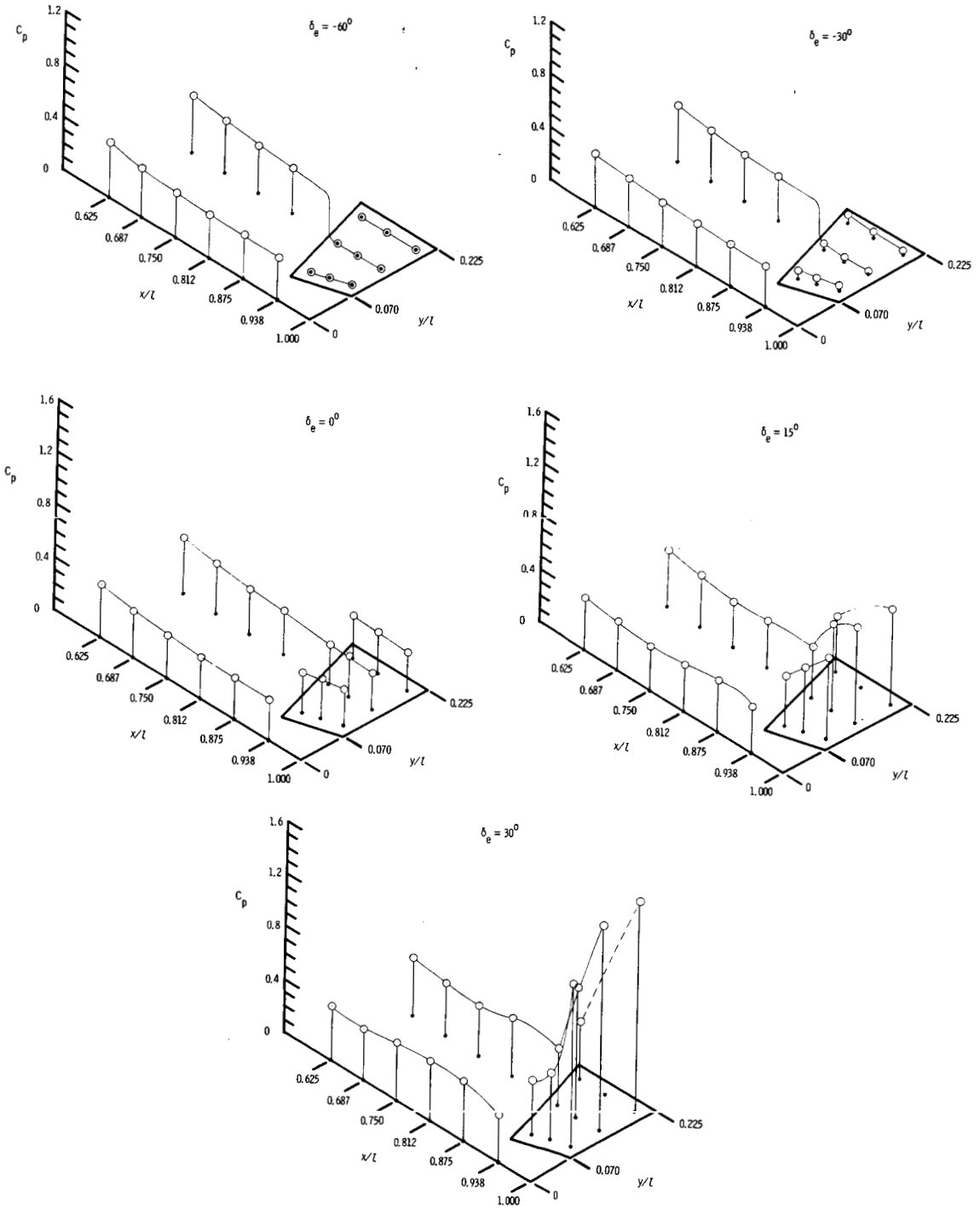

(b) $\alpha = 40^0$.

Figure 10.- Continued.

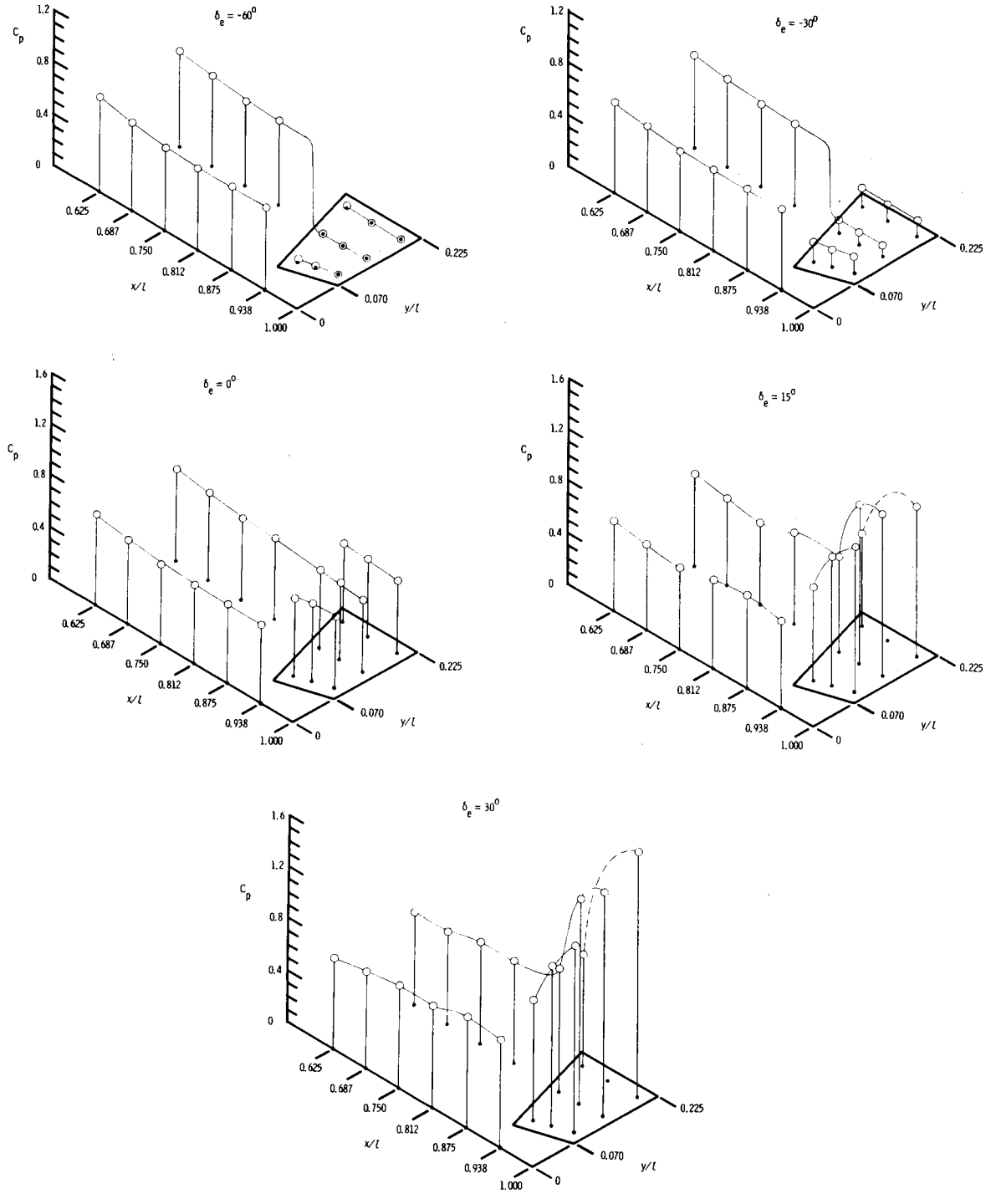

(c) $\alpha = 50^0$.

Figure 10.- Continued.

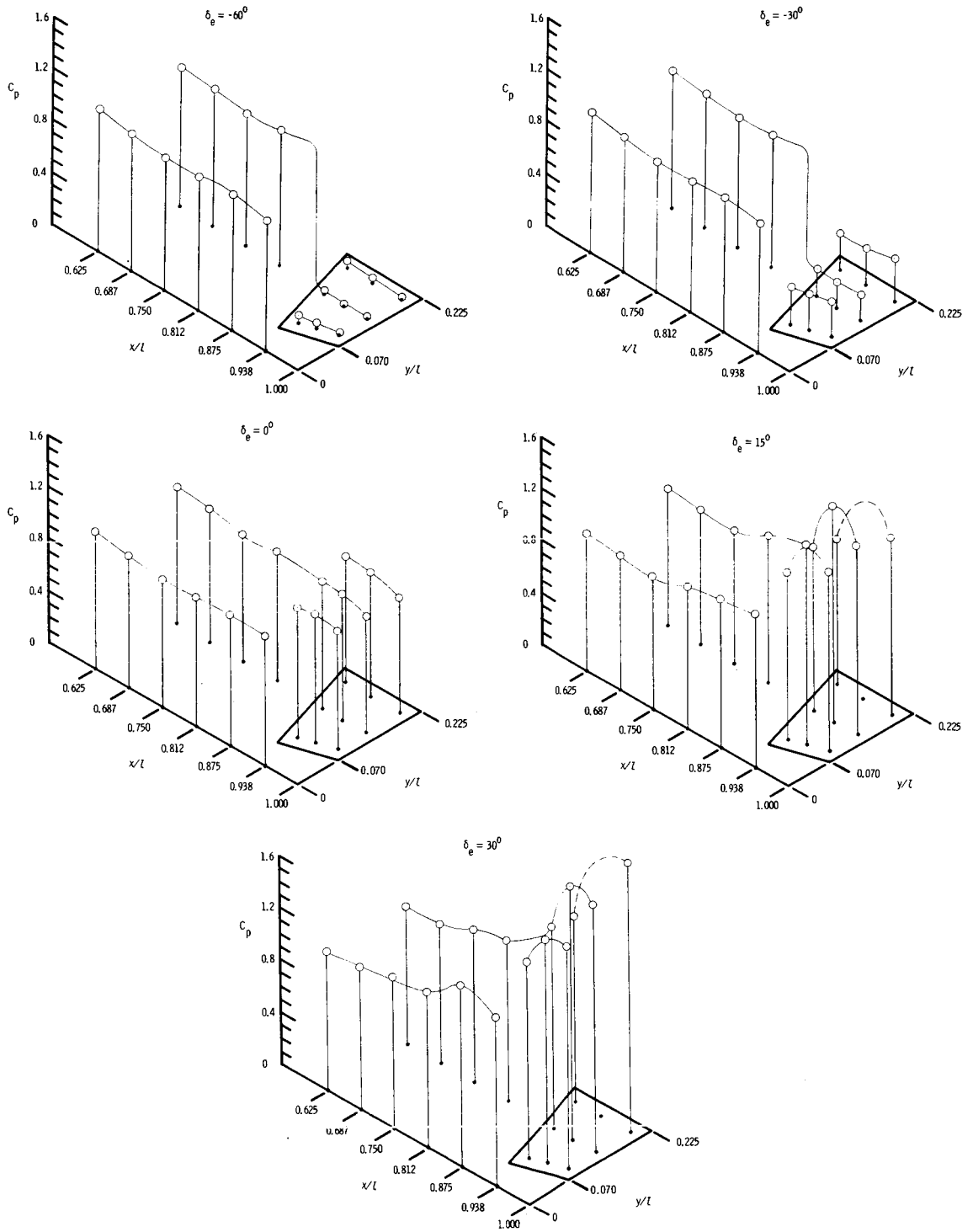

(d) $\alpha = 60^0$.

Figure 10.- Concluded.

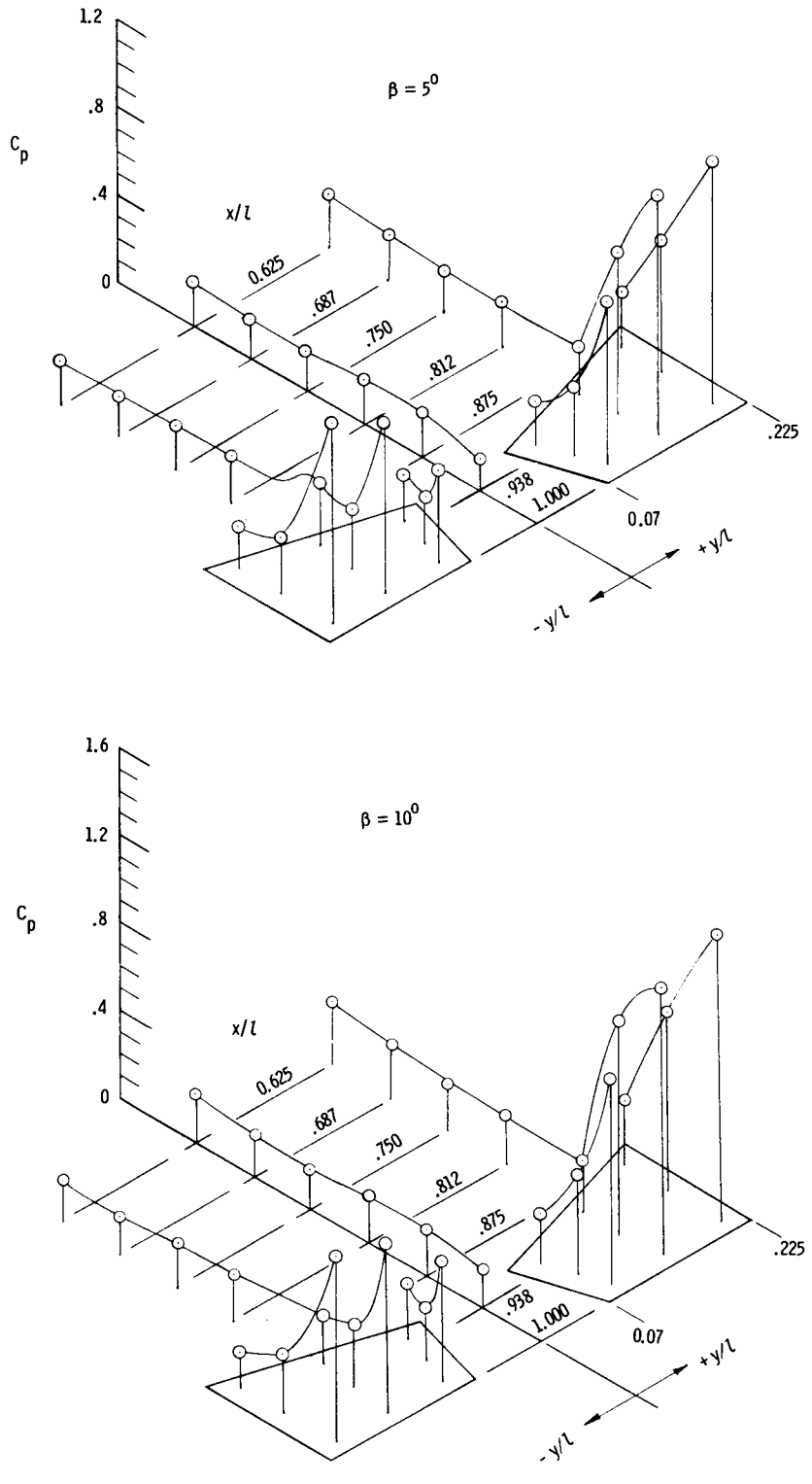

Figure 11.- Effect of sideslip angle on elevon and adjacent area pressure distributions at $\alpha = 30^0$, $\delta_e = 30^0$. $R = 1.5 \times 10^6$.

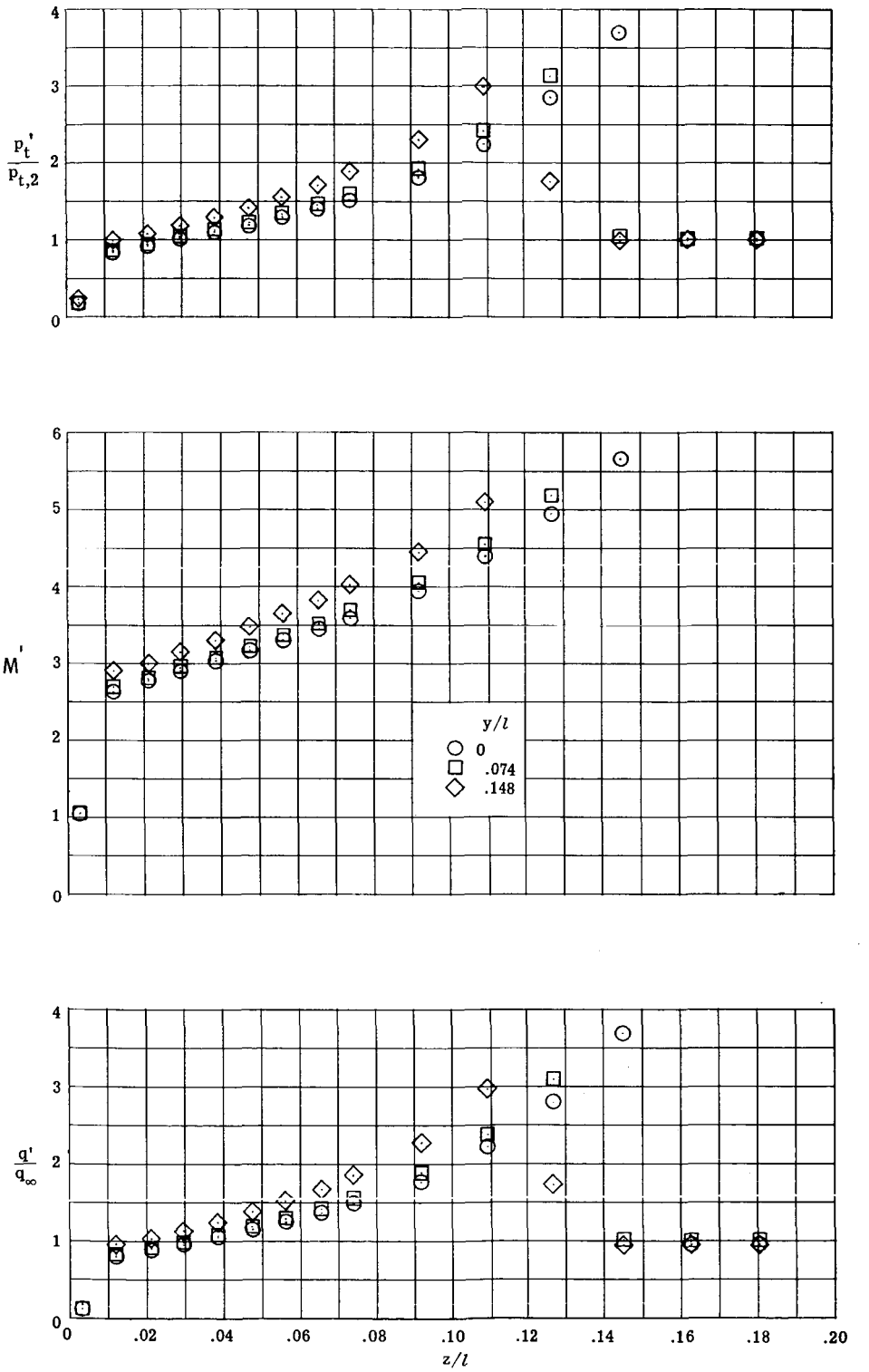

Figure 12.- Survey of flow field at $x/l = 0.812$. $\alpha = 30^0$; $\delta_e = 0^0$; $R = 1.5 \times 10^6$.

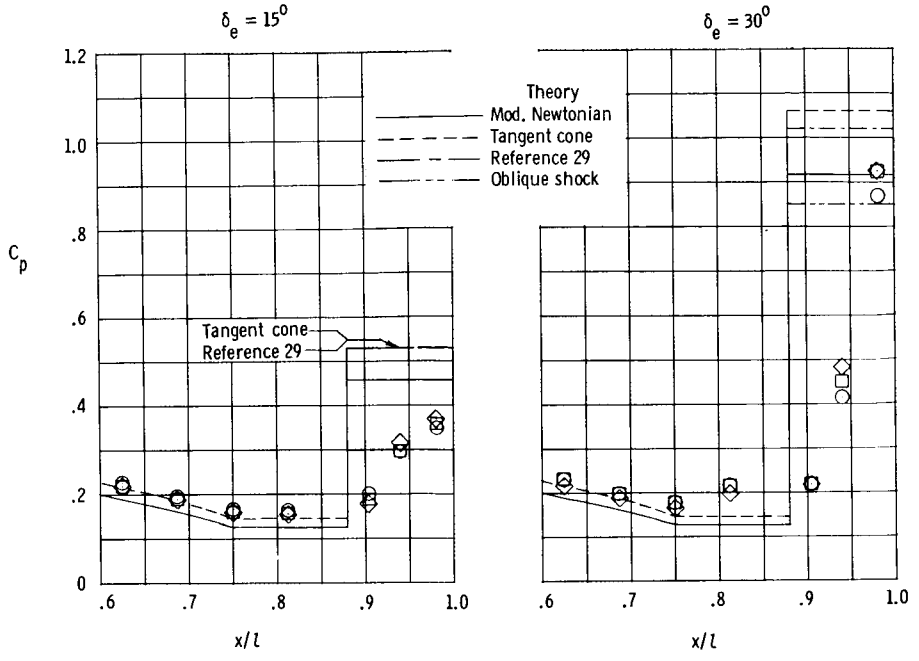

(a) $\alpha = 30^0$.

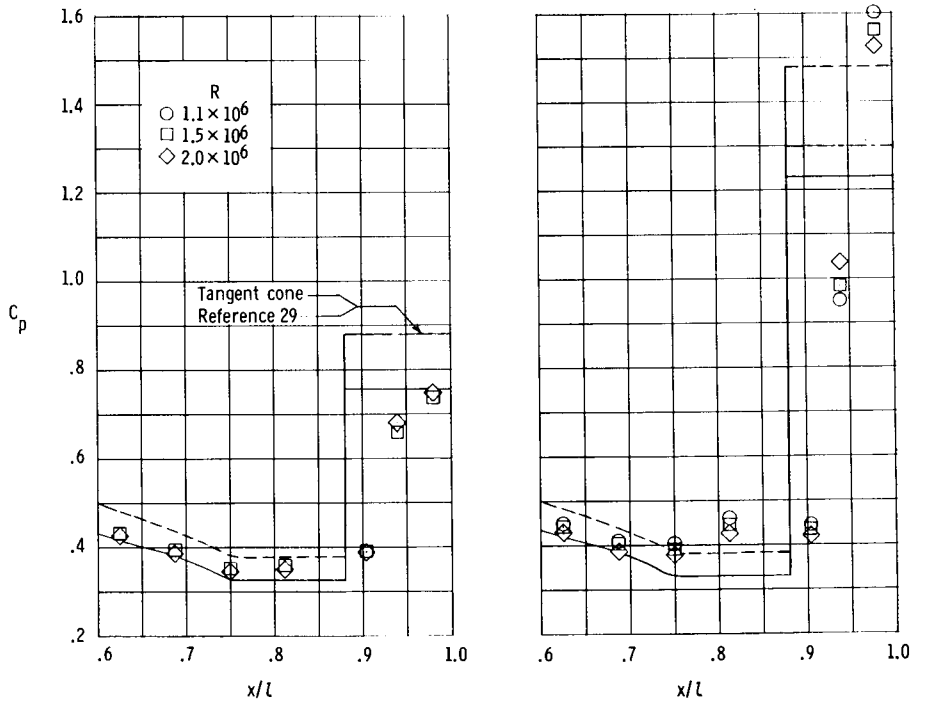

(b) $\alpha = 40^0$.

Figure 13.- Comparison of theoretical and experimental chordwise pressure distributions ahead of and on elevons at $\delta_e = 15^0$ and 30^0 for various angles of attack and Reynolds numbers.

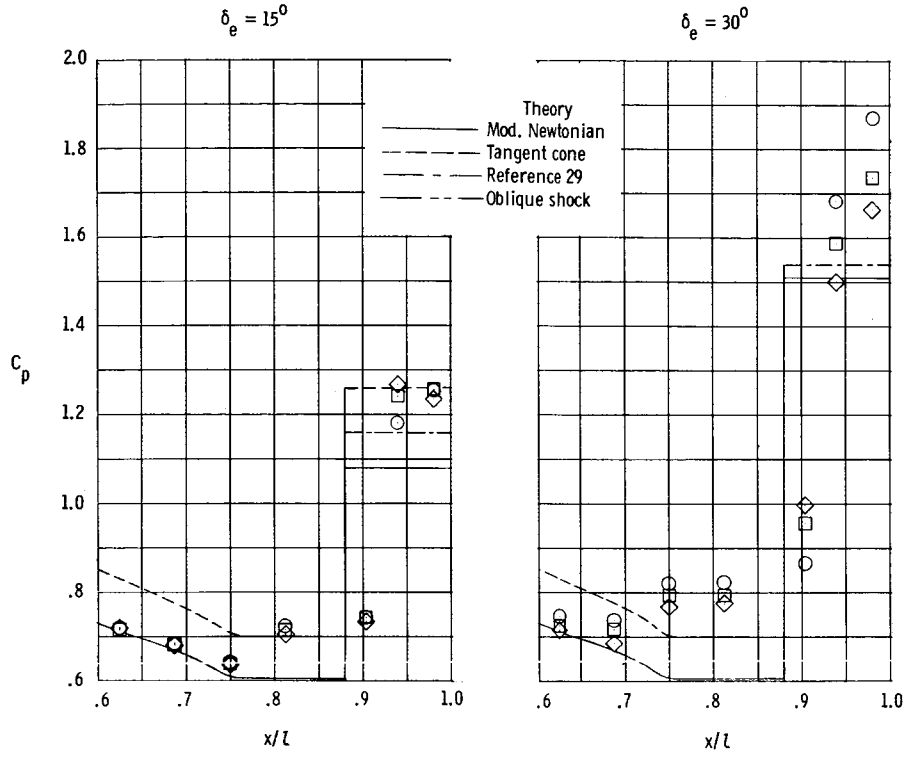

(c) $\alpha = 50^o$.

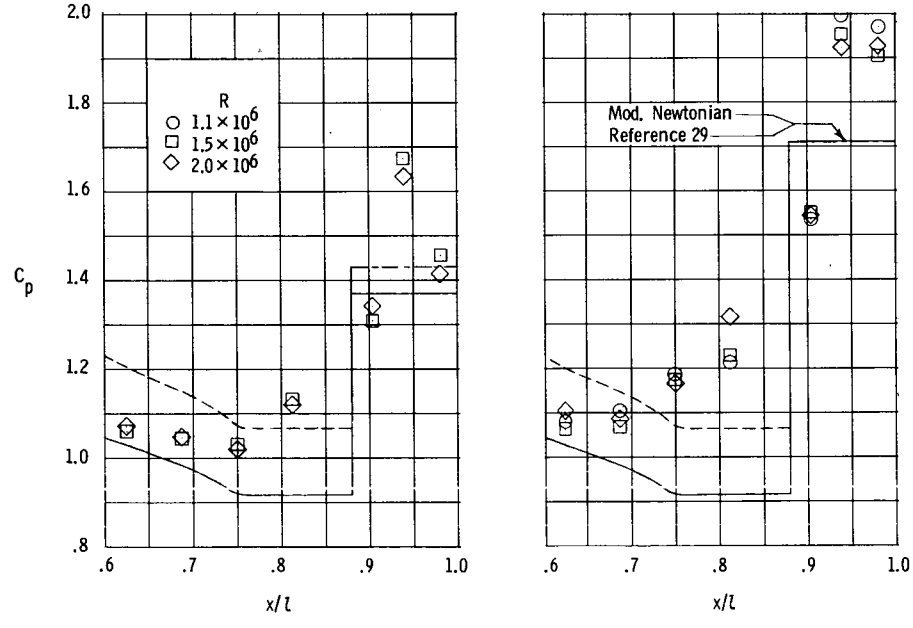

(d) $\alpha = 60^o$.

Figure 13.- Concluded.

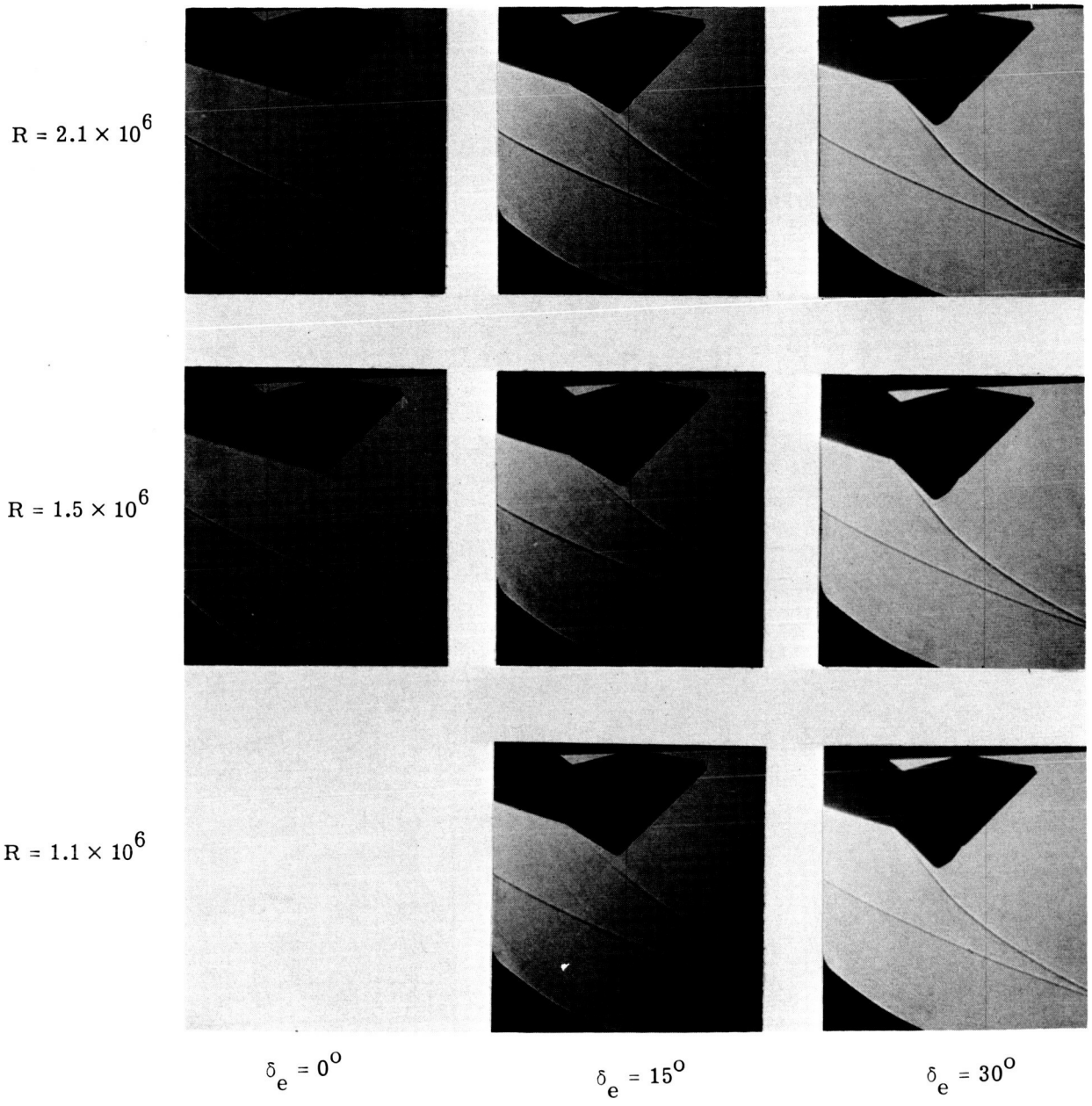

(a) $\alpha = 30^{\circ}$.

L-68-859

Figure 14.- Shadowgraph pictures of flow field in regions of elevons at $\delta_e = 0^{\circ}$, 15°, and 30° at various Reynolds numbers.

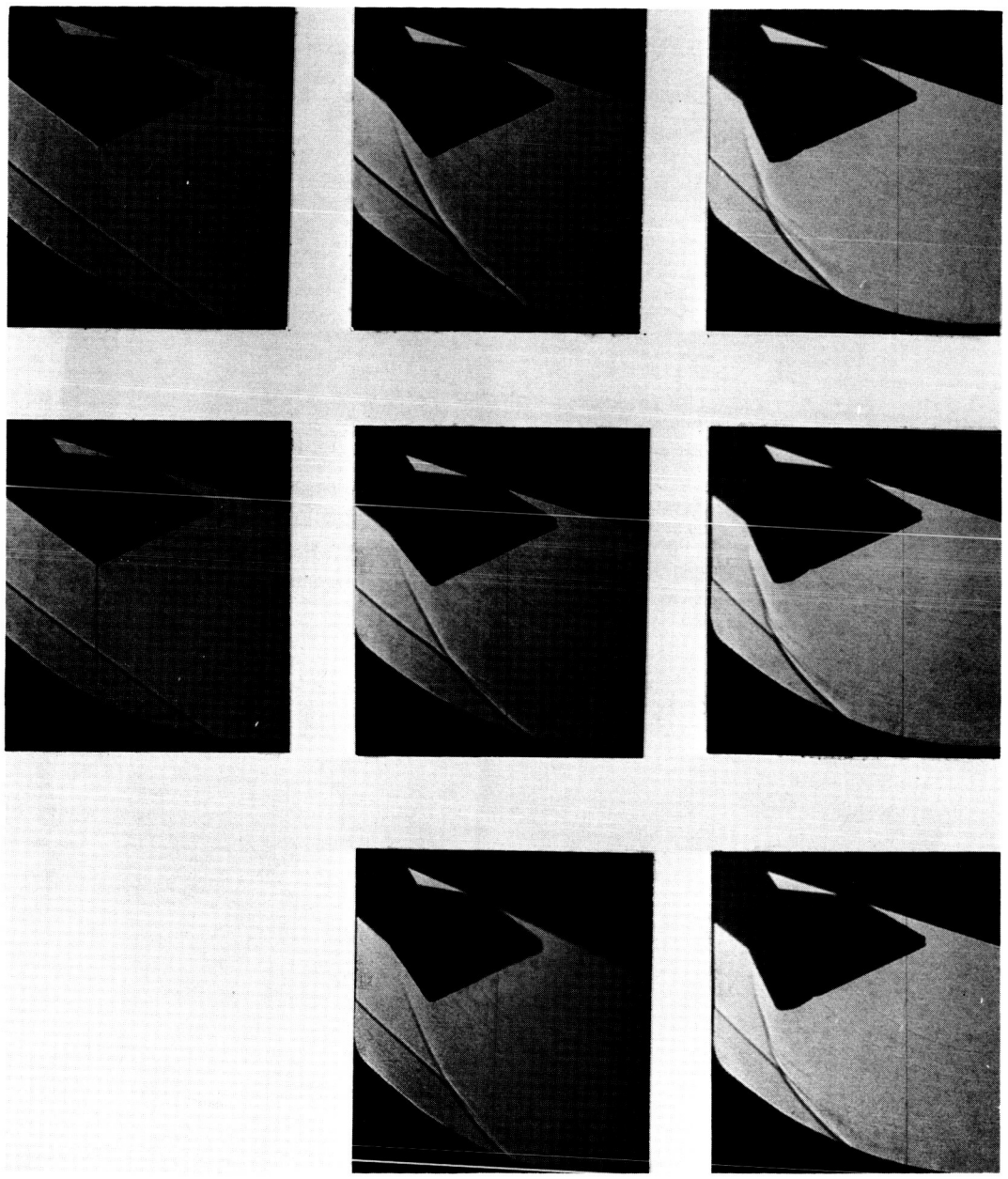

(b) $\alpha = 50^{\circ}$.

L-68-860

Figure 14.- Concluded.

"The aeronautical and space activities of the United States shall be conducted so as to contribute . . . to the expansion of human knowledge of phenomena in the atmosphere and space. The Administration shall provide for the widest practicable and appropriate dissemination of information concerning its activities and the results thereof."

—NATIONAL AERONAUTICS AND SPACE ACT OF 1958

NASA SCIENTIFIC AND TECHNICAL PUBLICATIONS

TECHNICAL REPORTS: Scientific and technical information considered important, complete, and a lasting contribution to existing knowledge.

TECHNICAL NOTES: Information less broad in scope but nevertheless of importance as a contribution to existing knowledge.

TECHNICAL MEMORANDUMS: Information receiving limited distribution because of preliminary data, security classification, or other reasons.

CONTRACTOR REPORTS: Scientific and technical information generated under a NASA contract or grant and considered an important contribution to existing knowledge.

TECHNICAL TRANSLATIONS: Information published in a foreign language considered to merit NASA distribution in English.

SPECIAL PUBLICATIONS: Information derived from or of value to NASA activities. Publications include conference proceedings, monographs, data compilations, handbooks, sourcebooks, and special bibliographies.

TECHNOLOGY UTILIZATION PUBLICATIONS: Information on technology used by NASA that may be of particular interest in commercial and other non-aerospace applications. Publications include Tech Briefs, Technology Utilization Reports and Notes, and Technology Surveys.

Details on the availability of these publications may be obtained from:

SCIENTIFIC AND TECHNICAL INFORMATION DIVISION

NATIONAL AERONAUTICS AND SPACE ADMINISTRATION

Washington, D.C. 20546